AGU PUBLICATIONS

JGR

Journal of Geophysical Research: Oceans

RESEARCH ARTICLE

10.1002/2014JC010224

Key Points:
- A new ocean color algorithm for optically shallow waters is described
- The algorithm was tested in waters of the Great Barrier Reef, Australia
- Shallow water effects are corrected using bathymetry and benthic albedo maps

Supporting Information:
- Readme
- Table S1
- Table S2
- Table S3
- Table S4
- Table S5
- Table S6
- Table S7

Correspondence to:
L. I. W. McKinna,
lachlan.i.mckinna@nasa.gov

Citation:
McKinna, L. I. W., P. R. C. Fearns, S. J. Weeks, P. J. Werdell, M. Reichstetter, B. A. Franz, D. M. Shea, and G. C. Feldman (2015), A semianalytical ocean color inversion algorithm with explicit water column depth and substrate reflectance parameterization, *J. Geophys. Res. Oceans*, *120*, 1741–1770, doi:10.1002/2014JC010224.

Received 9 JUN 2014
Accepted 31 JAN 2015
Accepted article online 6 FEB 2015
Published online 19 MAR 2015

A semianalytical ocean color inversion algorithm with explicit water column depth and substrate reflectance parameterization

Lachlan I. W. McKinna[1,2], Peter R. C. Fearns[2], Scarla J. Weeks[3], P. Jeremy Werdell[4], Martina Reichstetter[3], Bryan A. Franz[4], Donald M. Shea[4,5], and Gene C. Feldman[4]

[1]NASA Postdoctoral Program Fellow, Ocean Ecology Laboratory, NASA Goddard Space Flight Center, Greenbelt, Maryland, USA, [2]Remote Sensing and Satellite Research Group, Department of Imaging and Applied Physics, Curtin University, Perth, Western Australia, Australia, [3]Biophysical Oceanography Group, School of Geography, Planning and Environmental Management, University of Queensland, Queensland, Brisbane, Australia, [4]Ocean Ecology Laboratory, NASA Goddard Space Flight Center, Greenbelt, Maryland, USA, [5]Science Applications International Corporation, Greenbelt, Maryland, USA

Abstract A semianalytical ocean color inversion algorithm was developed for improving retrievals of inherent optical properties (IOPs) in optically shallow waters. In clear, geometrically shallow waters, light reflected off the seafloor can contribute to the water-leaving radiance signal. This can have a confounding effect on ocean color algorithms developed for optically deep waters, leading to an overestimation of IOPs. The algorithm described here, the Shallow Water Inversion Model (SWIM), uses pre-existing knowledge of bathymetry and benthic substrate brightness to account for optically shallow effects. SWIM was incorporated into the NASA Ocean Biology Processing Group's L2GEN code and tested in waters of the Great Barrier Reef, Australia, using the Moderate Resolution Imaging Spectroradiometer (MODIS) Aqua time series (2002–2013). SWIM-derived values of the total non-water absorption coefficient at 443 nm, $a_t(443)$, the particulate backscattering coefficient at 443 nm, $b_{bp}(443)$, and the diffuse attenuation coefficient at 488 nm, $K_d(488)$, were compared with values derived using the Generalized Inherent Optical Properties algorithm (GIOP) and the Quasi-Analytical Algorithm (QAA). The results indicated that in clear, optically shallow waters SWIM-derived values of $a_t(443)$, $b_{bp}(443)$, and $K_d(443)$ were realistically lower than values derived using GIOP and QAA, in agreement with radiative transfer modeling. This signified that the benthic reflectance correction was performing as expected. However, in more optically complex waters, SWIM had difficulty converging to a solution, a likely consequence of internal IOP parameterizations. Whilst a comprehensive study of the SWIM algorithm's behavior was conducted, further work is needed to validate the algorithm using in situ data.

1. Introduction

Over the past three decades, ocean color remote sensing has provided remarkable insight into physical, biological, and biogeochemical processes within the world's oceans. Spaceborne ocean color sensors, such as NASA's Moderate Resolution Imaging Spectroradiometer onboard Aqua (MODIS Aqua), provide synoptic-scale, spectral radiometric measurements of the ocean's color that can be directly related to the relative concentrations of optically active constituents within the water column. Hence, a series of empirical and physics-based algorithms have been developed that relate sensor-observed, spectral water-leaving radiometric measurements to marine components, such as phytoplankton and suspended particulate matter (SPM), to give quantitative estimates of their abundance/concentration. Much effort has focused on the development and continual improvement of ocean color algorithms for deep, oceanic waters for which the optically dominant constituent is typically phytoplankton. Such oceanic algorithms have been highly refined through use of decades-long dedicated in situ validation measurements collected by optical moorings and from ships-of-opportunity in accordance with strict data quality control and assurance protocols [*Mueller et al*., 2003]. As such, these algorithms are generally considered robust and have met original mission objectives for oceanic chlorophyll-a concentration (CHL) retrievals and spectral remote sensing reflectance (R_{rs}) accuracies to within ±35% and ±5%, respectively [*McClain*, 2009].

Presently, two challenges are being actively addressed in order to extend ocean color applications to coastal regions: (i) optically complex waters and (ii) optically shallow waters. In optically complex waters, the optical properties of the water column are typically influenced by nonalgal particulate matter, colored dissolved organic matter, and phytoplankton [*IOCCG*, 2000], and unlike oceanic waters, the nonalgal constituents do not necessarily covary with respect to phytoplankton abundance. Regarding optically shallow waters, these can be characterized as zones in which light reflected from the seafloor influences the water-leaving radiance signal [*Lee et al*., 1998] thereby confounding contemporary ocean color algorithms developed for optically deep waters [*Cannizzaro and Carder*, 2006; *Qin et al*., 2007; *Zhao et al*., 2013] (see Appendix A for further discussion). Whilst a range of ocean color algorithms have been developed and proven effective within optically complex waters [*Doerffer and Schiller*, 2007; *Lee et al*., 2002; *Smyth et al*., 2006; *Werdell et al*., 2013a], only a few approaches for optically shallow waters have been published [*Barnes et al*., 2014, 2013; *Brando et al*., 2012] with none in operation that explicitly use pre-existing water column depth and benthic albedo data sets to improve IOP retrievals.

A variety of shallow water inversion algorithms have been developed with much past research focused on the simultaneous retrieval of water column depth and benthic characterization [*Bierwirth et al*., 1993; *Dierssen et al*., 2003; *Louchard et al*., 2003; *Lyzenga*, 1978; *Philpot*, 1989; *Stumpf et al*., 2003; *Werdell and Roesler*, 2003]. Many recent approaches such as the Hyperspectral Optimization Process Exemplar (HOPE), a semianalytical inversion algorithm developed by *Lee et al*. [1998], and the Comprehensive Reflectance Inversion based on Spectrum matching and Table Look up (CRISTAL), a spectral matching look-up-table algorithm developed by *Mobley et al*. [2005], have been developed for simultaneous retrieval of bathymetry, benthic types, and IOPs. The HOPE algorithm and its variants (e.g., *Goodman and Ustin*, [2007]; ALUT—*Hedley et al*. [2009]; BRUCE—*Klonowski et al*. [2007]; SAMBUCA—*Wettle and Brando* [2006]) and CRISTAL have shown particular merit when applied to hyperspectral imagery (contiguous spectral bands, resolution ~5 nm) [*Brando et al*., 2009; *Dekker et al*., 2011; *Fearns et al*., 2011; *Garcia et al*., 2014a; *Goodman and Ustin*, 2007; *Hedley et al*., 2009; *Klonowski et al*., 2007; *Lee et al*., 1999; *Lesser and Mobley*, 2007]. However, these previous studies were designed primarily to demonstrate bathymetric retrieval and benthic classification capabilities for shallow waters, typically less than 10 m depth, with little emphasis on the derived IOP values and downstream geophysical products such as CHL, SPM, and water clarity measures.

Although hyperspectral sensors have previously been used for remote sensing optically shallow waters, such activities are usually targeted one-off surveys with narrow spatial coverage (in the order of 10–100 km^2) typically collected from airborne platforms. Conversely, most current spaceborne ocean color sensors are multispectral—with MODIS having seven spectral bands (~10 nm width) in the visible domain—and have near-daily repeat capture times with broad spatial swaths (in the order of 10^6 km^2). Whilst hyperspectral data preserve a great deal of radiometric information, a modeling study by *Lee and Carder* [2002] showed that the spectral resolution of the ocean color sensors: the Sea-viewing Wide Field-of-view Sensor (SeaWiFS), the Medium Resolution Imaging Spectrometer (MERIS), and MODIS were sufficient to produce reliable IOP and water column depth retrievals. Furthermore, a case study in Great Bahamas Bank showed that trustworthy bathymetry could be retrieved using the HOPE algorithm when applied to MERIS imagery [*Lee et al*., 2010]. Unfortunately, both MERIS and SeaWiFS have ceased operating, thus MODIS Aqua was selected for the development and implementation of a HOPE-based algorithm for optically shallow waters.

Here we present an approach for remote sensing optically shallow waters based on the HOPE semianalytical inversion algorithm. Our approach, named the Shallow Water Inversion Model (SWIM), explicitly includes bathymetry and benthic albedo maps as auxiliary data sets. We have selected the Great Barrier Reef (GBR) as the test region for algorithm development and evaluation as the bathymetry, and the benthic properties of this shallow shelf region are well characterized. Within this paper, we: (i) detail the structure of the SWIM algorithm, (ii) present a brief overview of algorithm performance based on radiative transfer modeling, (iii) demonstrate how the inclusion of depth and benthic albedo influences IOP retrievals in a MODIS Aqua test scene, (iv) using the full MODIS Aqua archive, compare SWIM-derived IOPs to those derived using the Generalized IOP (GIOP) [*Werdell et al*., 2013a] and Quasi-Analytical Algorithm (QAA) [*Lee et al*., 2002] optically deep ocean color algorithms, and (v) discuss the relative performance and limitations of the SWIM algorithm. Unfortunately, in situ IOP data for the GBR could not be sourced at the time of writing this paper. As such, in situ validation of SWIM's accuracy is beyond the scope of this research.

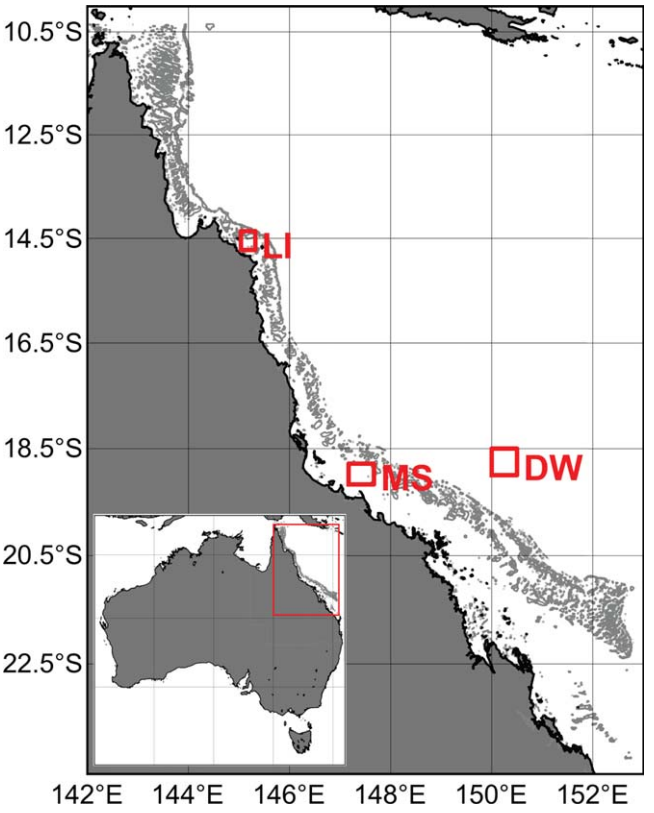

Figure 1. Map of the Great Barrier Reef region. Light gray features offshore outline the coral reef matrix. The red boxes labeled "LI," "DW," and "MS" represent the "Lizard Island," "Deep Water," and "Mid-Shelf" regions examined in time series analysis. Transects were examined within the LI region.

2. Methods and Data

2.1. Test Region: The Great Barrier Reef

The GBR, shown in Figure 1, is located along the north-east coast of Australia and is the largest coral reef ecosystem in the world, extending ~2300 km from 9°S to 24°S. The GBR comprises approximately 3000 individual coral reefs, 600 continental islands, is designated as a UNESCO World Heritage Area, and is encompassed by Australia's largest marine park, a region spanning 344,400 km^2. Recently, concerns about the ecosystem health of the GBR, linked to declining water quality [*Brodie et al*., 2012], led to the establishment of government-funded programs such as the Reef Water Quality Protection Plan (RWQPP; http://www.reefplan.qld.gov.au/) and the Reef Rescue Water Quality Monitoring Program (http://www.nrm.gov.au/funding/reef-rescue/). The aim of these programs is to halt and reverse the decline in the quality of water flowing into the GBR, supported by continual monitoring of water quality conditions in the region. Because of its synoptic-scale spatial coverage and near-daily over-pass frequency, ocean color remote sensing has become an integral part of monitoring and reporting spatiotemporal trends in water quality for the GBR region [*Brando et al*., 2011; *Devlin et al*., 2012; *Devlin and Schaffelke*, 2009; *Fabricius et al*., 2014; *Schroeder et al*., 2012; *Weeks et al*., 2012].

2.2. Semianalytical Inversion Algorithm

Semianalytical ocean color inversion algorithms, SAAs, are designed to retrieve IOPs from sensor-observed above-water remote sensing reflectances, R_{rs}. Spectral-matching-type SAAs comprise three components: (i) a forward reflectance model, (ii) spectral IOP models, and (iii) an inverse solution (matching) method. The forward model analytically approximates the remote sensing reflectance, R_{rs}^{mod}, which is then compared using some similarity metric (e.g., Chi-squared, Euclidean distance) to the sensor-observed spectra, R_{rs}^{obs}. The magnitude of the spectral IOPs in the forward model are then iteratively adjusted by an inverse solution method (e.g., an optimization algorithm) that attempts to match R_{rs}^{mod} with R_{rs}^{obs}. The spectral matching algorithm stops once R_{rs}^{mod} is deemed to best represent R_{rs}^{obs}, at which point the set of IOPs used to compute the optimal R_{rs}^{mod} are returned as the solution.

2.2.1. Forward Reflectance Models

Typically, optically deep SAAs are based on a robust relationship between the subsurface remote sensing reflectance, $r_{rs}(\lambda)$, the total absorption, $a(\lambda)$, and total backscattering, $b_b(\lambda)$, coefficients developed by *Gordon et al*. [1988]

$$r_{rs}(\lambda) \approx \sum_{i=1}^{2} g_i \left(\frac{b_b(\lambda)}{b_b(\lambda)+a(\lambda)} \right)^i \quad (\mathrm{sr}^{-1}), \tag{1}$$

where the coefficients g_1 and g_2 vary with solar and sensor-viewing geometries, in-water scattering phase functions, bidirectional reflectance effects, and sea surface conditions [*Gordon et al*., 1988;

Morel et al., 2002]. To convert modeled subsurface remote sensing reflectance to above-water remote sensing reflectance values, the following relationship is used,

$$R_{rs}^{\mathrm{mod}}(\lambda)=\frac{\Gamma r_{rs}^{\mathrm{mod}}(\lambda)}{1-\zeta r_{rs}^{\mathrm{mod}}(\lambda)} \quad (\mathrm{sr}^{-1}), \tag{2}$$

where $\zeta = 0.5$ and $\Gamma = 1.5$ [*Lee et al*., 1998, 1999].

2.2.2. Spectral IOP Models

The bulk IOPs—$a(\lambda)$ and $b_b(\lambda)$—used in the SAA are each expressed as the sum of the absorption and backscattering coefficients of optically active constituent matter in the water column

$$a(\lambda)=a_w(\lambda)+a_\phi(\lambda)+a_{dg}(\lambda) \quad (\mathrm{m}^{-1}), \tag{3}$$

$$b_b(\lambda)=b_{bw}(\lambda)+b_{bp}(\lambda) \quad (\mathrm{m}^{-1}), \tag{4}$$

where the subscripts, *w*, ϕ, *p*, and *dg* represent water itself, phytoplankton, particulate matter, and colored dissolved and detrital matter, respectively. The spectral values of $a_w(\lambda)$ and $b_{bw}(\lambda)$ are known and treated as constants [*Pope and Fry*, 1997; *Zhang et al*., 2009] whilst the spectral shapes of $a_{dg}(\lambda)$ and $b_{bp}(\lambda)$ can be modeled using exponential and power law functions, respectively [*Bricaud et al*., 1981; *Carder et al*., 1999], as

$$a_{dg}(\lambda)=Ge^{-S(\lambda-443)} \quad (\mathrm{m}^{-1}), \tag{5}$$

$$b_{bp}(\lambda)=X\left(\frac{443}{\lambda}\right)^{\gamma} \quad (\mathrm{m}^{-1}), \tag{6}$$

where *G* and *X* are scaling factors, each corresponding to the magnitudes of $a_{dg}(443)$ and $b_{bp}(443)$. The exponential slope coefficient for $a_{dg}(\lambda)$, *S*, and the power law coefficient of $b_{bp}(\lambda)$, γ, are typically set within the ranges of 0.01–0.025 and 0.0–2.0, respectively, based on accepted literature values [*Carder et al*., 1999; *Roesler et al*., 1989]. The spectral shape of $a_\phi(\lambda)$ used within an SAA is often normalized to 1.0 at 443 nm. The normalized phytoplankton absorption coefficient, $a_\phi^*(\lambda)$, can be a single fixed spectral shape [*Maritorena et al*., 2002] or modeled using basis vectors [*Bricaud et al*., 1998; *Ciotti and Bricaud*, 2006; *Lee et al*., 1998]. The resulting parameterization of $a_\phi(\lambda)$ within an SAA thus takes the form

$$a_\phi(\lambda)=Pa_\phi^*(\lambda) \quad (\mathrm{m}^{-1}), \tag{7}$$

where *P* is a scaling factor corresponding to the magnitude of $a_\phi(443)$.

2.2.3. Solution Method

A spectral matching solution method commonly employed by SAA algorithms is a nonlinear least squares optimization routine such as the Levenberg-Marquardt, L-M, algorithm [*Moré*, 1977]. In order to retrieve IOPs for a sensor-observed pixel, the L-M routine minimizes a cost function, *err*, which compares how similar $R_{rs}^{\mathrm{obs}}(\lambda)$ is relative to $R_{rs}^{\mathrm{mod}}(\lambda)$

$$err=\sqrt{\sum\left[R_{rs}^{obs}(\lambda)-R_{rs}^{\mathrm{mod}}(\lambda)\right]^2}, \tag{8}$$

where $R_{rs}^{\mathrm{mod}}(\lambda)$ is a function of three free parameters

$$R_{rs}^{\mathrm{mod}}(\lambda)=\mathrm{f}(P,G,X) \quad (\mathrm{sr}^{-1}). \tag{9}$$

The scalar parameters *P*, *G*, and *X* representing the magnitude of the IOPs are iteratively varied until the desired convergence criteria is met (i.e., *err*, equation (8), is minimized below a prescribed threshold). Using hyperspectral data, *Garcia et al*. [2014b] found an *err* threshold in the order of 1×10^{-5} was suitable. For SWIM, the L-M *err* threshold was set to 1×10^{-6}. This value was selected by testing MODIS Aqua inversions over a range of *err* thresholds (results not shown). We note that setting *err* too large may cause L-M convergence to local minima, whereas setting *err* too small may cause the preset number of iterations to be exceeded. Once convergence occurs, L-M stops and values of *P*, *G*, and *X* are returned as the "best fit" IOP solution. If the convergence criterion is not met, or the preset maximum number of L-M iterations of 1000 is exceeded, a product failure solution flag (PRODFAIL) is returned.

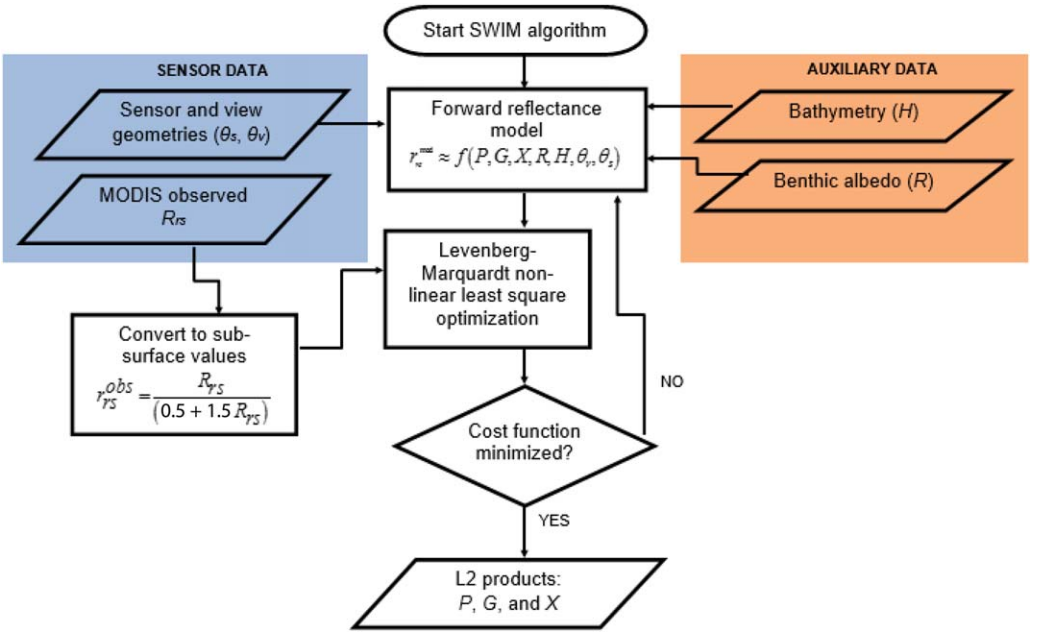

Figure 2. Flowchart diagram of the SWIM algorithm. Blue shaded data indicate MODIS Aqua sensor data while orange shaded data identify auxiliary data required by the SWIM algorithm.

The L-M algorithm requires an initial "best guess" of the IOP parameters *P*, *G*, and *X*. Past implementations of the HOPE algorithm have used both scene-wide fixed initial guesses [*Lee et al*., 2001] and pixel-wise variable initial guesses based on empirical relationships with R_{rs} [*Dekker et al*., 2011; *Lee et al*., 1999]. Within the SWIM algorithm, scene-wide fixed initial guesses of 0.2, 0.01, and 0.001 m^{-1} were used for *P*, *G*, and *X*, respectively. These initialization values are similar to those used previously when applying the HOPE algorithm and its variants [*Garcia et al*., 2014a; *Klonowski et al*., 2007] and are similar to initial guesses used in the default parameterization of GIOP [*Werdell et al*., 2013a]. It has been established that initial guess used in the L-M optimization can affect the retrieved IOPs, particularly if the starting guess is next to a local solution space minima [*Garcia et al*., 2014b]. *Garcia et al*. [2014b] demonstrated that Latin Hypercube Sampling (LHS) of the solution space aided in finding a set of best guess parameters that reduced the occurrence of local solution minima. However, the LHS method of *Garcia et al*. [2014b] was not in mature form at the time of writing this paper and thus was not considered for use within the SWIM algorithm.

2.3. Shallow Water Inversion Model (SWIM)

The SWIM algorithm has the same structure as a typical SAA described in section 2.2 but differs in the forward reflectance model used. This section provides a description of the SWIM SAA, which uses a shallow water reflectance model to account for the combined effects of water column depth and benthic albedo (reflectance). GBR-specific bathymetric and benthic albedo data sets were used as forward reflectance model inputs. A nearest-neighbor resampling scheme was implemented to extract corresponding bathymetry and benthic albedo data for a given MODIS Aqua pixel. A schematic flowchart of the SWIM algorithm is shown in Figure 2.

2.3.1. Shallow Water Reflectance Model

For optically shallow waters, forward reflectance models relating IOPs and $r_{rs}(\lambda)$ have been developed using quasi-single scattering theory [*Lyzenga*, 1978; *Maritorena et al*., 1994; *Philpot*, 1987]. These were further refined by *Lee et al*. [1998] to explicitly incorporate IOPs and both solar and sensor geometries,

$$r_{rs}(\lambda) \approx r_{rs}^{dp}(\lambda) - r_{rs}^{dp}(\lambda) exp\left\{-\left[k_d(\lambda)+k_u^C(\lambda)\right]H\right\} + \frac{\rho(\lambda)}{\pi} exp\left\{-\left[k_d(\lambda)+k_u^B(\lambda)\right]H\right\} \quad (sr^{-1}), \tag{10}$$

where *H* is the water column depth, $\rho(\lambda)$ is the benthic albedo (reflectance) coefficient, $r_{rs}^{dp}(\lambda)$ is the remote sensing reflectance of optically deep water (as in equation (1)), $k_d(\lambda)$ is the downwelling diffuse attenuation coefficient, $k_d^C(\lambda)$ is the upwelling diffuse attenuation for radiance scattered from the water column, and

$k_d^B(\lambda)$ is the upwelling diffuse attenuation coefficient for radiance reflected off the benthos [*Lee et al*., 1998]. The diffuse attenuation coefficients are functions of the IOPs and solar and sensor geometries and are expressed according to *Lee et al*. [1998, 1999] as

$$k_d(\lambda)=\frac{\kappa(\lambda)}{cos\theta_S} \quad (m^{-1}), \tag{11}$$

$$k_u^C(\lambda)=\frac{1.03\,\kappa(\lambda)[1+2.4\,\kappa(\lambda)]^{0.5}}{cos\theta_v} \quad (m^{-1}), \tag{12}$$

$$k_u^B(\lambda)=\frac{1.04\,\kappa(\lambda)[1+5.4\,\kappa(\lambda)]^{0.5}}{cos\theta_v} \quad (m^{-1}), \tag{13}$$

where θ_s is subsurface solar zenith angle, θ_v is the subsurface-viewing angle from nadir, and $k(\lambda)$ is expressed as

$$\kappa(\lambda)=a(\lambda)+b_b(\lambda) \quad (m^{-1}). \tag{14}$$

Thus, using equation (10), the *Lee et al*. [1998, 1999] shallow water forward model computes $R_{rs}^{mod}(\lambda)$ as a function of seven scalar parameters,

$$R_{rs}^{mod}(\lambda)=f(P,G,X,R,H,\theta_s,\theta_v) \quad (sr^{-1}), \tag{15}$$

where the scalars *P*, G, X, and *R* are the magnitudes of $a_\phi(443)$, $a_{dg}(443)$, $b_{bp}(443)$, and the benthic albedo coefficient at 550 nm, $\rho(550)$, and the parameter *H* corresponds to the water column depth. The parameters $\theta_s$and θ_v are the subsurface solar zenith angle and the subsurface-viewing angle from nadir respectively, both of which are treated as known values. The number of free variables in the forward model can be reduced if known sensor/solar geometries, bathymetry, and benthic albedo data are used as inputs. The shallow water forward model thus can take the form of equation (9) and becomes a function of only three unknown IOP parameters: *P*, *G*, and *X*.

Within this study, we have parameterized the spectral IOPs within the shallow water forward model as follows: the spectral slope of $a_{dg}^*(\lambda)$, $S = 0.017$, and the power exponent of $b_{bp}^*(\lambda)$, $\gamma = 1.0$. The values of γ and *S* were selected based on previous research in the GBR test region [*Blondeau-Patissier et al*., 2009; *Brando et al*., 2009, 2012]. A region-specific $a_\phi^*(\lambda)$ was used with further details given in Appendix B.

2.3.2. Bathymetry Data

Bathymetric data used for testing SWIM in the GBR were extracted from a spatially consistent, gridded digital elevation model data set (vertical datum: MSL; horizontal datum: WGS-84), 3D-GBR [*Beaman*, 2010]. The 3D-GBR data set is a composite of nearly 9.5×10^8 xyz data points sourced from multibeam and single-beam acoustic soundings, Royal Australian Navy airborne Light Detecting and Ranging (LiDAR) data, Shuttle Radar Topographic Mission (SRTM) data, and coastline data [*Beaman*, 2010]. The resulting 3D-GBR data set has a pixel resolution of 100 m × 100 m, and was deemed to resolve bathymetric features with sufficient horizontal and vertical detail for use as a SWIM algorithm input. Figure 3 shows the 3D-GBR digital elevation map of the GBR region and demonstrates both the extent of shallow shelf waters (less than 30 m) and also the large offshore reef matrix on the outer continental shelf. The 3D-GBR data set was downloaded from the Great Barrier Reef online e-atlas website (http://eatlas.org.au/data/uuid/200aba6b-6fb6–443e-b84b-86b0bbdb53ac).

2.3.3. Benthic Albedo Map

Marine benthic communities in the GBR are complex and spatially varied. As such, it was a challenge constructing a data set suitable for characterizing the benthic albedo of the entire region. A pragmatic approach to the problem was to begin simply with just two benthic classes: "light" and "dark," each with their own benthic albedo spectrum, $\rho_L(\lambda)$ and $\rho_D(\lambda)$, respectively. The net benthic albedo per-pixel, $\rho_{net}(\lambda)$, was then calculated via a linear mixing model

$$\rho_{net}(\lambda)=c_L\rho_L(\lambda)+c_D\rho_D(\lambda) \tag{16}$$

where c_L and c_D are the relative proportion of light and dark benthic classes for a given pixel. Whilst not within the scope of this paper, it should be noted that further improvements to the benthic reflectance

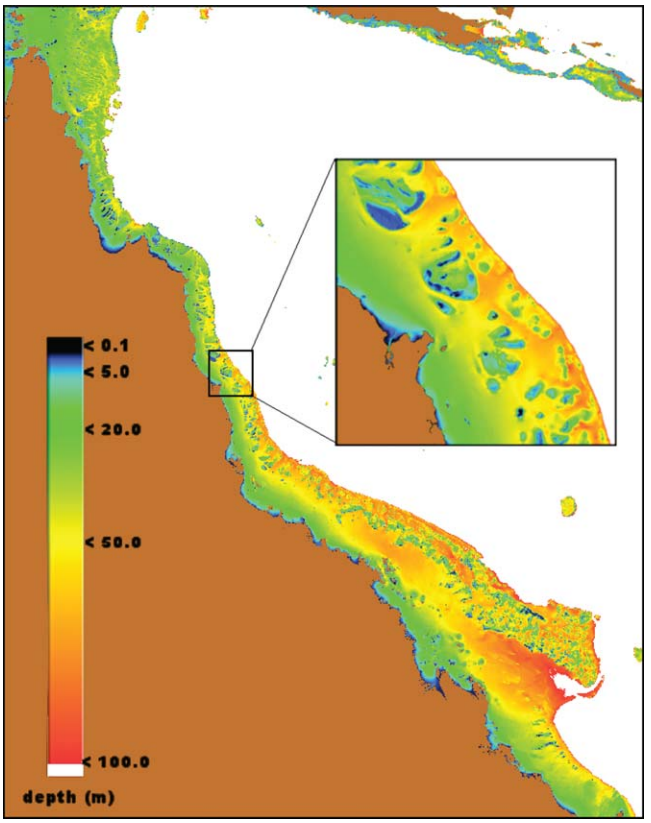

Figure 3. The 3D-GBR [*Beaman*, 2010] 100 × 100 m bathymetry map of the Great Barrier Reef region (below mean sea level). The subset shown demonstrates how well fine-scale features are resolved by the data set. Note that brown is land and white denotes regions that are deeper than 100 m.

class map are envisioned and it is mathematically feasible to include more than two classes in the SWIM algorithm.

In order to map the relative proportions of light and dark substrates, a comprehensive seabed biodiversity habitat data set compiled by the Commonwealth Scientific and Industrial Research Organization, CSIRO, was used [*Pitcher et al*., 2007]. The data set comprises approximately 1500 individual data points, spanning an area of 210,000 km^2. At each sampling location, the bottom was characterized using data collected by a variety of instruments including: a digital acoustic sounder, baited remote underwater video stations (BRUVS), an epibenthic sled and trawl, and towed video and digital cameras. Data were collected on numerous research cruises over a cumulative period of approximately 10 months resulting in almost 100,000 photographs, 1150 BRUVS videos, over 600 km of towed video, and 140 GB of digital echograms [*Pitcher et al*., 2007].

In order to develop the two-class benthic type map, all habitat types were first qualitatively categorized as either "light" or "dark" (see Table 1). This was conducted by examining photographic and written descriptions of each habitat type. Typically, habitat types deemed as "light" were dominated by sand, whereas those classified as "dark" had denser proportions of nonsand vegetative material such as algae, coral, seagrass, and Halimeda. Second, at each data point, the relative proportion of light-to-dark substrate was calculated resulting in two maps: (i) proportion of light substrates and (ii) proportion of dark substrates. Third, both maps were spatially interpolated using ArcGIS geospatial software [*ESRI*, 2011] to a raster grid using an inverse weighted interpolation tool. The resultant light and dark maps were produced with pixel resolutions of 100 × 100 m, projected to the WGS-84 datum, to be spatially consistent with the 3D-GBR bathymetry grid. Finally, an albedo spectrum was constructed for each benthic type (i.e., light and dark). This was done by assigning the most appropriate benthic albedo spectrum from a precompiled spectral reflectance library [*Leiper et al*., 2011; *Roelfsema and Phinn*, 2012] to each biodiversity type listed in Table 1. The multiple albedo spectra assigned to each class (Table 1) were then averaged together resulting in two separate ("dark" and "light") albedo spectra as shown in Figure 4. The resultant benthic albedo map is available online from PANGEA® earth and environmental science data publishing service [*Reichstetter et al*., 2014].

Table 1. Partitioning of CSIRO Great Barrier Reef Biodiversity Benthic Habitat Types as Described by *Pitcher et al.* [2007] Into Dark and Light Categories

Dark Habitat Types	Light Habitat Types
Alcyonarians dense	No biohabitat
Whip Garden Dense	Bioturbated
Gorgonian Garden Dense	Alcyonarians sparse
Sponge Garden Dense	Alcyonarians medium
Hard Coral Garden Dense	Whip garden sparse
Live Reef Corals	Whip garden medium
Flora	Gorgonian garden sparse
Algae	Gorgonian garden medium
Halimeda	Sponge garden sparse
Caulerpa	Sponge garden medium
Seagrass	Hard coral garden sparse
	Hard coral garden medium
	Bivalve shell beds
	Squid eggs
	Tube Polychaete beds

2.3.4. Constrained L-M Solution Method

In this study, we used *levmar*, a C-based version of the L-M, optimization routine [*Lourakis*, 2003], to perform nonlinear least squares curve fitting. Further, the magnitude of the IOP parameters (*P*, *G*, and *X*) in the L-M routine were constrained using upper and lower bounds following *Garcia et al*. [2014a],

$$-0.05a_w(443) < P < 5.0 \quad (\mathrm{m}^{-1}), \tag{17}$$

$$-0.05a_w(443) < G < 5.0 \quad (\mathrm{m}^{-1}), \tag{18}$$

$$-0.05b_w(443) < X < 5.0 \quad (\mathrm{m}^{-1}), \tag{19}$$

where the lower bounds are −5% of the absorption or backscattering coefficient of pure water. These bounds were based on the range of IOP retrievals considered valid by *Werdell et al*. [2013a] in a study of deep water ocean color algorithm parameterization. A comprehensive discussion of using constrained L-M optimization with a shallow water inversion algorithms can be found in *Garcia et al*. [2014b]. Note, PRODFAIL flags were not assigned to L-M solutions that settled on lower or upper boundaries. However, any such values were identified and excluded during post-processing.

2.4. Algorithm Evaluation

The SWIM algorithm was added to the NASA Ocean Biology Processing Group L2GEN satellite data processing code (packaged as part of the SeaWiFS Data Analysis System (SeaDAS); http://oceancolor.gsfc.nasa.gov). This enabled efficient comparison of SWIM-derived data products with those from the GIOP and QAA algorithms. Unfortunately, quantitative matchup validation analysis using in situ IOP measurements was not possible due to a lack of sufficient available data for the GBR region. As such, we have conducted a brief study using radiative transfer modeling to ascertain the expected quality of SWIM, GIOP, and QAA retrievals in optically shallow waters. Further comparisons between SWIM and GIOP/QAA were conducted using three test regions and the entire MODIS Aqua time series. It should be noted that the time series analyses did not provide an absolute assessment of the SWIM algorithm's retrieval accuracy, they did however facilitate quantitative relative comparisons between SWIM and GIOP/QAA using a temporally rich data set.

2.4.1. Radiative Transfer Modeling

A brief theoretical study was conducted based on Hydrolight-Ecolight 5.1 (HE5) [*Mobley and Sundman*, 2008] radiative transfer code using a set of known IOPs to simulate R_{rs} corresponding to the spectral bands of MODIS Aqua. Using the resultant IOP/R_{rs} data set, the retrieval skill of SWIM, GIOP, and QAA was tested. Our modeling approach closely followed that of IOCCG Report 5 [*IOCCG*, 2006] and used the report's synthesized IOP data set (http://www.ioccg.org/groups/OCAG_data.html). Only the first 250 IOP combinations from the IOCCG's synthesized data set were used, corresponding to a CHL concentration range of 0.03–1.0 mg m^{-3}, a range deemed typical for the GBR. An optically deep scenario was first modeled using HE5 followed by four optically shallow scenarios modeled with geometric depths of 5, 10, 15, and 20 m and using the "dark" benthic albedo spectra presented in section 2.3.3 to represent the seafloor. Details of HE5 parameterization can be found in supporting information Table ts01.

From the simulated R_{rs} spectra, the absorption and backscattering coefficients at 443 nm and diffuse attenuation coefficients at 488 nm, $K_d(488)$, (as detailed in Table 2) were derived using SWIM, GIOP, and QAA and compared with the exact values. Inversion and analysis of HE5 data was conducted using implementations of SWIM, GIOP, and QAA written in the Python programming language. We chose to exclude both pure water absorption and backscattering coefficients (which were constant across all inversion algorithms) from IOP retrieval comparisons. Specifically, we considered the particulate backscatter coefficient at 443 nm, $b_{bp}(443)$, and total nonwater absorption coefficient at 443 nm, $a_t(443)$, where

$$a_t(443) = a_\varphi(443) + a_{dg}(443) \quad (\mathrm{m}^{-1}). \tag{20}$$

Note that $K_d(488)$ was computed from derived total absorption and backscattering coefficients at 488 nm, $a(488)$ and $b_b(488)$, respectively, using the model developed by *Lee et al*. [2005]

$$K_d(488) = m_0 a(488) + m_1 \left(1 - m_2 e^{-m_3 a(488)}\right) b_b(488) \quad (\mathrm{m}^{-1}), \tag{21}$$

where, $m_0 = 1 + 0.005\ \theta_s$, $m_1 = 4.18$, $m_2 = 0.52$, and $m_3 = 10.8$.

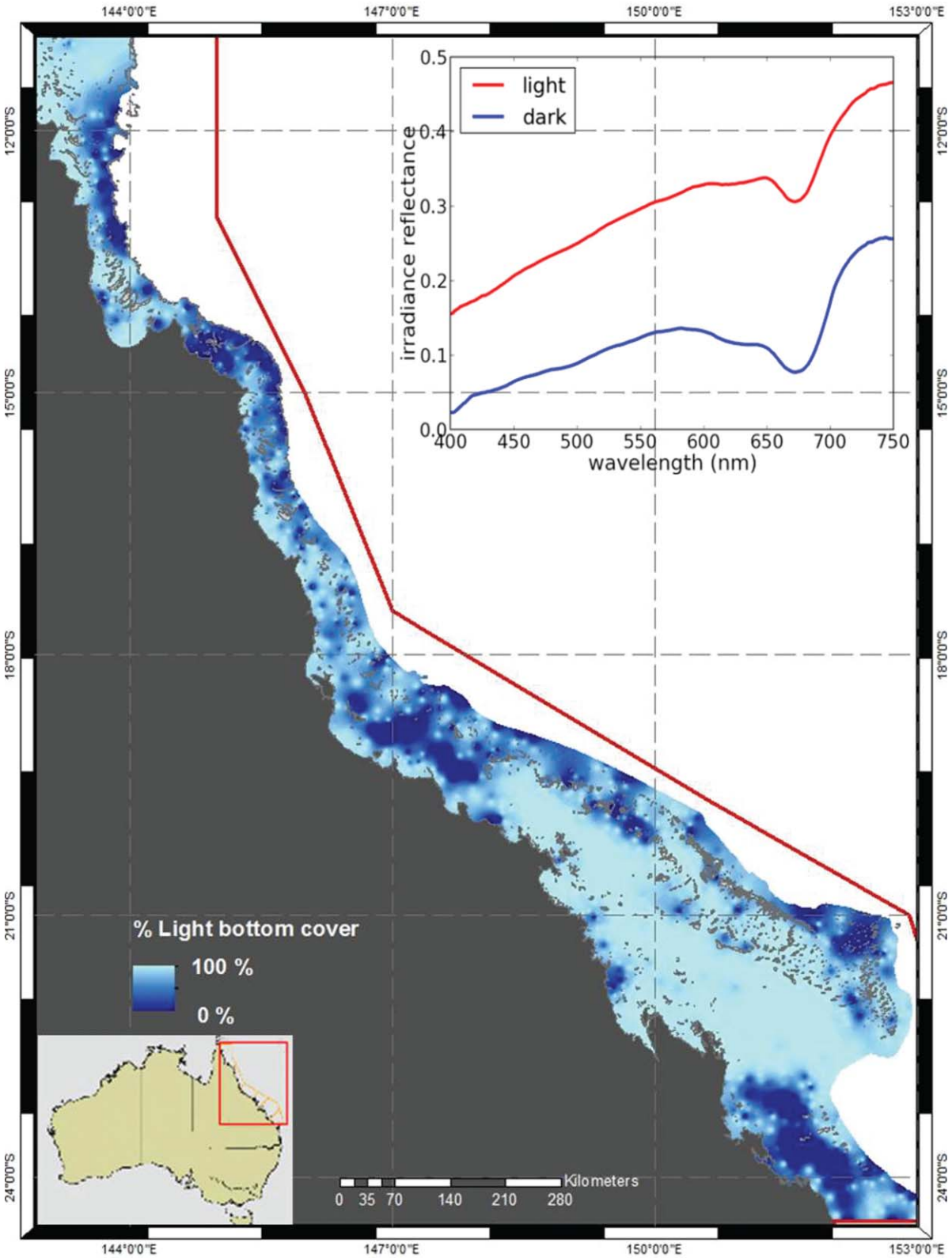

Figure 4. The "light" substrate-type percentage cover map. Regions dominated by "light" substrate types include river mouths, the mid-shelf and most of the coastal zone, which are likely to be sediment dominated. Darker regions are those having substrate types such as seagrass, coral, algae, and Halimeda. The irradiance reflectance (albedo) of the "light" and "dark" substrate types is presented in the top right.

Table 2. Optical Parameters of Interest Derived Using the SWIM, GIOP, and QAA Algorithms

Level-2 Products	Symbol	Units
Total nonwater absorption coefficient at 443 nm[a]	$a_t(443)$	m^{-1}
Backscattering coefficient of particulate matter at 443 nm	$b_{bp}(443)$	m^{-1}
Diffuse attenuation coefficient at 488 nm using Lee's IOP-centered model [*Lee et al.*, 2005]	$K_d(488)$	m^{-1}

[a]Here the total nonwater absorption coefficient at 443 nm, $a_t(443)$, refers to the sum of the absorption coefficients of phytoplankton, $a_\varphi(443)$, and colored dissolved and detrital matter, $a_{dg}(443)$.

2.4.2. MODIS Aqua Processing and Analysis

For this study, all MODIS Aqua Level-1A files that included any part of the GBR spatial domain {10°S–15°S, 142°E–155°E} were identified for batch processing. The Level-1A time series spanned June 2002 to September 2013, as per the 2013.0 MODIS Aqua Reprocessing data set. All MODIS Aqua data had at-nadir pixel resolutions of 1 km × 1 km. Approximately 7300 high-quality MODIS Aqua scenes remained after quality assurance screened out scenes with 80% or more cloud and/or sunglint contaminated pixels. These remaining scenes were processed from Level-1A to Level-2 using L2GEN and its standard atmospheric correction scheme [*Ahmad et al.*, 2010; *Bailey et al.*, 2010], an approach which has been identified as robust for optically complex waters such as those of Chesapeake Bay, USA [*Werdell et al.*, 2010]. We acknowledge that the standard L2GEN atmospheric correction has not formally been tested over optically shallow waters. This warrants further analysis beyond the scope of this paper. However, it was expected that any biases in R_{rs} introduced by suboptimal atmospheric correction procedure would be propagated as a systematic error of equal magnitude to all three inversion algorithms (GIOP, QAA, and SWIM). The L2 products derived using L2GEN were $a_t(443)$, $b_{bp}(443)$, and $K_d(488)$.

Following batch processing, Level-2 product statistics for each test region were extracted, including the mean, standard deviation, and number of valid pixels. Any pixels located partially or fully within a test region were excluded from analysis if they possessed one or more of L2GEN's default Level-2 quality control flags detailed in Table 3. For monthly calculations, means and standard deviations were weighted by the number of valid pixels in order to reduce biases due to missing data.

2.4.3. Single Test Scene: Northern GBR

A small geographic subset of a single MODIS Aqua image was selected for initial evaluation and demonstration of the SWIM algorithm. The test scene was captured on 22 May 2009, a day with minimal cloud cover and limited influence of smoke/dust. Cross-shelf east-west (E-W) and south-north (S-N) transects were used to examine how $a_t(443)$, $b_{bp}(443)$ and $K_d(488)$ retrievals varied with depth and benthic brightness, using SWIM, GIOP, and QAA. The selected test scene lies in the northern GBR and extends from Cape Melville southward to Cape Flattery {14.14°S–15.35°S, 144.36°E–146.05°E} (located in the vicinity of the "LI" region in Figure 1).

2.4.4. Time Series Test Regions

Three test regions were selected in order to compare SWIM, QAA, and GIOP under different water column, bathymetric, and benthic substrate conditions. We refer to these three subregions of the GBR as: "Deep Water" (DW), Lizard Island" (LI), and "Mid-Shelf" (MS), respectively. Specifically, the latitude and longitude ranges of the DW, LI, and MS were {18.5°S–19.038°S, 150.0°E–150.5°E}, {14.36°S–14.72°S, 145.04°E–145.32°E}, and {18.78°S–19.17°S, 147.17°E–147.67°E}, respectively (see Figure 1). The DW region was selected to examine how closely SWIM converged toward optically deep solutions in oceanic waters where the geometric depth exceeds the optical depth. The LI region was selected to gauge the relative performance of SWIM in very clear waters with bright benthos. The MS region was selected to determine how well SWIM performed in deeper mid-shelf waters that are often optically complex and are influenced by suspended sediment events. The bathymetry and benthos of the three test regions are summarized in Table 4.

3. Results and Discussion

3.1. Radiative Transfer Study

3.1.1. Retrieval Results

Radiative transfer modeling provided an accurate set of IOP/R_{rs} data thereby facilitating direct quantitative assessment of SWIM, GIOP, and QAA in optically shallow waters. Plots of algorithm-derived $a_t(443)$, $b_{bp}(443)$ and $K_d(488)$ compared to actual values are shown in Figure 5. The accompanying regression statistics are

Table 3. Level-2 Flags Used for Determining Pixels to be Excluded From Analysis

Flag Name	Description
ATMFAIL	Atmospheric correction failure
CLDICE	Probable cloud or ice contamination
HIGLINT	High sun glint
HILT	Observed radiance is very high or saturated
HISATZEN	High sensor view zenith angle
LAND	Pixel is over land
LOWLW	Very low water-leaving radiance
MAXAERITER	Aerosol iterations exceeded maximum number
STRAYLIGHT	Straylight contamination is likely

extensive, and as such are detailed in supporting information Tables ts02–ts04. A summary of the mean percent biases (MPB) for each set of retrievals is given in Table 5. When considering the optically deep scenario (first row of Figure 5), we observed that SWIM, GIOP, and QAA perform similarly at retrieving $a_t(443)$, $b_{bp}(443)$, and $K_d(488)$ evidenced by R^2 values >0.97 and mean ratios close to 1.0. Notably, retrievals of $b_{bp}(443)$ were slightly overestimated by all three algorithms at low values (<0.0015 m^{-1}). We infer these imperfect $b_{bp}(443)$ retrievals in very clear waters may be due to temperature-salinity effects on pure water scattering and/or due to Raman scattering not being accounted for in all three inversion algorithms [*Werdell et al*., 2013b; *Westberry et al*., 2013].

SWIM retrievals of $a_t(443)$ and $K_d(488)$ at 20, 15, and 10 m were good, evidenced by R^2 values > 0.93, regression slopes ranging from 0.87 to 0.99, and mean percent biases (MPB) ranging from 0 to 7% (see Table 5). However, the mean percent difference (MPD) gradually increased with decreasing water column depth from approximately 10% at 20 m to 22% at 10 m. SWIM retrievals of $b_{bp}(443)$ were reasonably good for water column depths of 20 and 15 m with corresponding R^2 of 0.91 and 0.80, regression slopes of 0.82 and 0.73, and mean ratios of 1.0 and 1.0, respectively. SWIM-derived $b_{bp}(443)$ values at 10 and 5 m became biased high particularly when $b_{bp}(443) < 0.003$ m^{-1}, and the corresponding regression statistics indicated these retrievals were not of highest quality evidenced by R^2 values of 0.53 and 0.44, regression slopes of 0.55 and 0.39, MPB of 5 and 28%, and MPD of 47 and 87%, respectively. At water column depths of 5 m, SWIM-derived values of $a_t(443)$ and $K_d(488)$ tended to be biased slightly high for clearer waters (i.e., where, $a_t(443) < 0.04$ m^{-1} and $K_d(488) < 0.07$ m^{-1}). Nonetheless, the regression statistics of SWIM-derived $a_t(443)$ and $K_d(488)$ at 5 m indicated reasonable retrieval skill with R^2 values of 0.91 and 0.89, mean slopes of 0.77 and 0.74, MPB of 16 and 16%, and MPD of 38% and 30%, respectively.

GIOP and QAA retrievals of $a_t(443)$ and $K_d(488)$ at 20, 15, 10, and 5 m had R^2 values ranging between 0.73 and 0.97 and slopes ranging between 0.25 and 0.85. Notably, a distinct increase in positive bias was observed as the water column depth decreased (see both Figure 5 and Table 5). Specifically, at depths of 20, 15, 10, and 5 m, the MPBs of GIOP/QAA-derived $a_t(443)$ and $K_d(488)$ were approximately 25, 40, 80, and 200%, respectively. GIOP and QAA retrievals of $b_{bp}(443)$ at depths of 20, 15, and 10 m, had R^2 values ranging between 0.49 and 0.85, and regression slopes ranging between 0.14 and 0.53. MPB values of retrieved $b_{bp}(443)$ were approximately 38, 67, and 240% at depths of 20, 15, and 10 m, respectively. At a water column depth of 5 m, both GIOP and QAA retrievals of $b_{bp}(443)$ were poor, evidenced by low R^2 (<0.35), flattened mean slopes (<0.05), MPBs in excess of 300%, and large MPD values (>650%).

3.1.2. Interpretation of Results

The results from the HE5-based theoretical study indicated that SWIM, GIOP, and QAA performed comparatively well for optically deep waters, retrieving $a_t(443)$, $b_{bp}(443)$, and $K_d(488)$ with good precision and minimal bias. For the optically shallow scenarios, SWIM performed well relative to GIOP and QAA when retrieving $a_t(443)$ and $K_d(488)$. The regression statistics also showed SWIM retrievals of $b_{bp}(443)$ were better than GIOP and QAA at depths of 20 and 15 m. However, at depths less than 10 m, the regression statistics alone suggest that SWIM-derived $b_{bp}(443)$ were biased high. However, we note that biases in SWIM-retrieved $b_{bp}(443)$ occurred mainly at low backscattering values (<0.003 m^{-1}) and overall SWIM retrievals of $b_{bp}(443)$ at 10 and 5 m were still improved relative to those of GIOP and QAA. Distinct positive biases in

Table 4. Bathymetry and Benthic Characteristics of the Four Regions Selected for Testing SWIM

Test Region	Mean Depth (m)	Mean Light/ Dark Benthic Proportions (%)	Mean $\rho(550)$	Benthic Description
Deep Water (DW)	1700	—	—	—
Lizard Island (LI)	18	48/52	0.206	Mix of sand, abundant seagrass, and corals
Mid-shelf (MS)	44	49/51	0.208	Sparse seagrass and coarse sediments

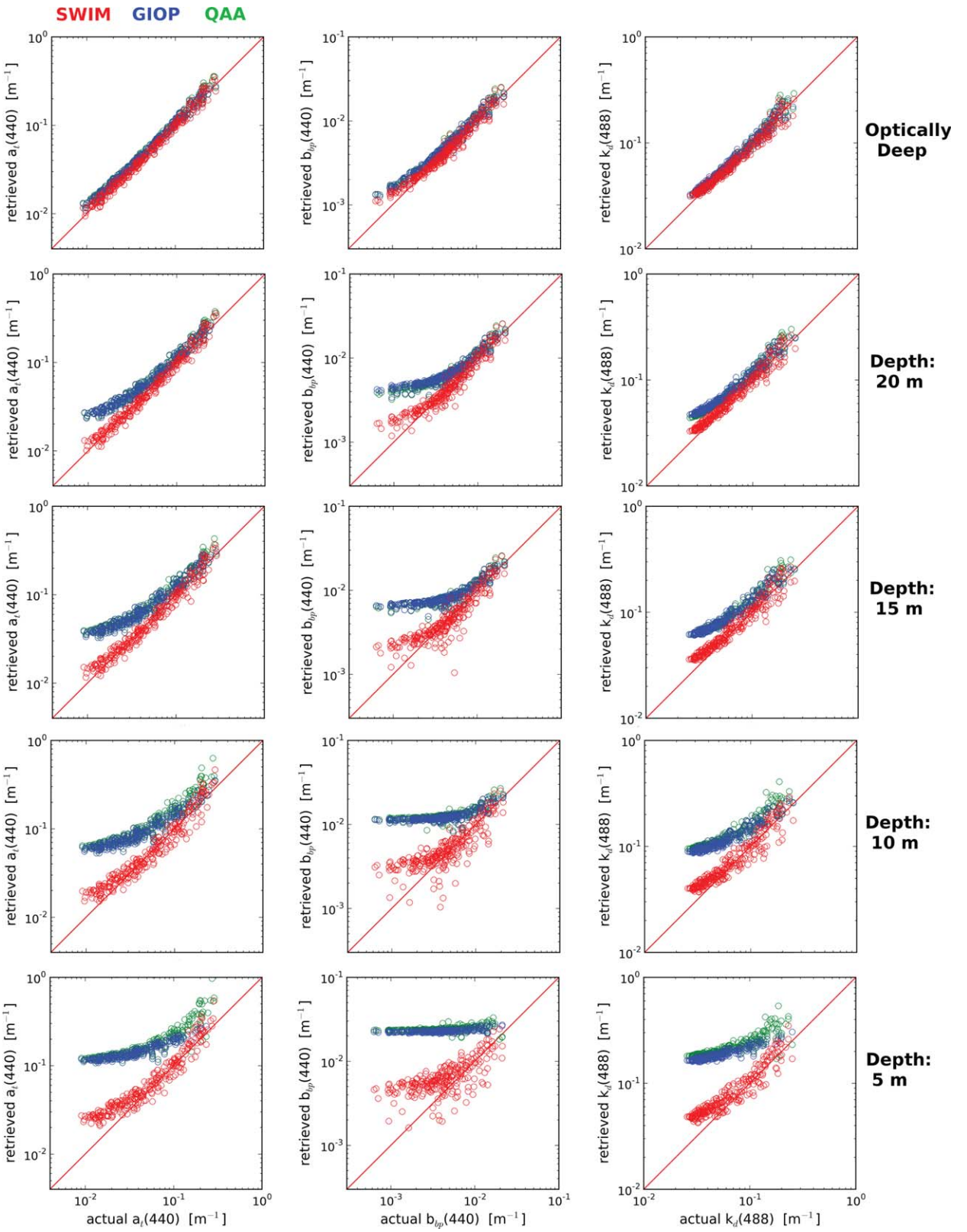

Figure 5. Comparison plots of algorithm-derived parameters (SWIM: red, GIOP: blue, and QAA: green) and actual values from the synthesized data set. From left-to-right, the three columns represent the optical parameters: $a_t(443)$, $b_{bp}(443)$, and $K_d(488)$. Rows from top-to-bottom correspond to decreasing water column depth.

Table 5. Mean Percent Bias in Algorithm Retrievals Oversimulated Optically Shallow Waters[a]

		Mean Percent Bias (%)		
	Depth (m)	$a_t(443)$	$b_{bp}(443)$	$K_d(488)$
SWIM	Optically deep	2	0	−4
	20	0	0	4
	15	0	0	4
	10	6	5	7
	5	16	28	16
GIOP	Optically deep	2	11	2
	20	22	38	26
	15	39	67	42
	10	82	242	83
	5	107	374	213
QAA	Optically deep	14	15	4
	20	25	38	25
	15	42	67	42
	10	85	241	83
	5	177	344	197

[a]Mean percent bias calculated from mean ratios detailed in supporting information Tables ts02–ts04.

retrieved values were noted for GIOP and QAA for all optically shallow scenarios, with relative biases in derived $b_{bp}(443)$ being consistently larger than those for $a_t(443)$ and $K_d(488)$. An important outcome from this analysis was an understanding of algorithm biases in optically shallow waters. Such information was deemed necessary for the interpretation of MODIS Aqua time series retrievals.

To interpret the consistent overestimation of IOPs in shallow waters made by GIOP and QAA, it is useful to consider the structure of each algorithm. Whilst the mathematical solution method and internal IOP parameterization of GIOP and QAA differ, the same semianalytical model for optically deep water [*Gordon et al*., 1988] forms the basis of both algorithms [*Lee et al*., 2002; *Werdell et al*., 2013a]. Thus, for GIOP and QAA, the magnitude and spectral shape of $r_{rs}(\lambda)$ is essentially dependent upon a ratio of $b_b(\lambda)$-to-$a(\lambda)$. Therefore, for optically shallow waters where benthic reflectance contributes to $r_{rs}(\lambda)$, mathematically GIOP and QAA would likely interpret this effect as increased $b_{bp}(\lambda)$ accompanied by increased $a_t(\lambda)$. When examining results of the radiative transfer study, the hypothesized overestimation of $b_{bp}(443)$ and $a_t(443)$ by GIOP and QAA in optically shallow waters was clearly evident. As a consequence of GIOP and QAA overestimating $a_t(\lambda)$ and $b_{bp}(\lambda)$, subsequent calculations of $K_d(488)$ using the IOP-centered approach of *Lee et al*. [2005] were also overestimated.

3.2. Test Scene: Northern Great Barrier Reef

3.2.1. Retrieval Results

The true color image denoted as "RGB" in Figure 6 provides a good indication of the spatial complexity that occurs within waters of the GBR. Waters adjacent to the coast and on the mid-shelf appear "greenish" and turbid. Further eastward, the water appears to become "bluer" toward the continental shelf edge where distinct barrier coral reef structures can be seen. Beyond the continental shelf edge (depth $>$ 1000 m), the water appears darker blue. A comprehensive description of the benthic composition and sedimentology in this region can be found in "bioregions" maps (http://www.gbrmpa.gov.au/__data/assets/pdf_file/0004/25906/gbrmpa_bioregions_2001_06.pdf) developed by the Great Barrier Reef Marine Park Authority's Representative Areas Program (http://www.gbrmpa.gov.au/zoning-permits-and-plans/rap/research-and-planning), with further detail reported by both *Matthews et al*. [2007] and *Pitcher et al*. [2007]. In the northern GBR test region (Figure 6), the nearshore zone adjacent to the coastline is characterized by low nutrients and minimal river outflow with a benthos comprising sand with low carbonate, and very dense seagrass and coastal coral reefs often occurring in places. The mid-shelf benthos tends to be muddy with dense seagrass beds, and has a number of small, vegetated islands with fringing coral reefs. The outer-shelf edge is characterized by carbonate sand, medium densities of seagrass and sponges, and large barrier reef structures that are separated by deep channels.

Subplots in the first row of Figure 6, denoted as "depth" and "$\rho(550)$," show bathymetric and benthic albedo features. A band of water less than 10 m in depth occurs adjacent to the coastline, and a broad region approximately 15 m in depth occurs toward the center of the scene. A wide region of brightest benthic albedo, $\rho(550) \approx 0.27$, occurs in the southern third of the scene, whereas the albedo becomes less toward the central/upper part of the scene where $\rho(550)$ ranges between 0.15 and 0.2. Note, some interpolation artifacts are present in the benthic $\rho(550)$ plot, apparent as circular spatial patches. When examining retrievals of $a_t(443)$, $b_{bp}(443)$, and $K_d(488)$ in Figure 6, SWIM-derived parameters appear lower in nearshore shallow waters ($<$15 m) relative to those of GIOP and QAA. Furthermore, in deep offshore waters where bottom reflectance is negligible, retrievals of $a_t(443)$, $b_{bp}(443)$, and $K_d(488)$ by SWIM appear very similar to those of GIOP/QAA. Note, increasing water clarity in the offshore direction was expected [*Blondeau-Patissier et al*., 2009].

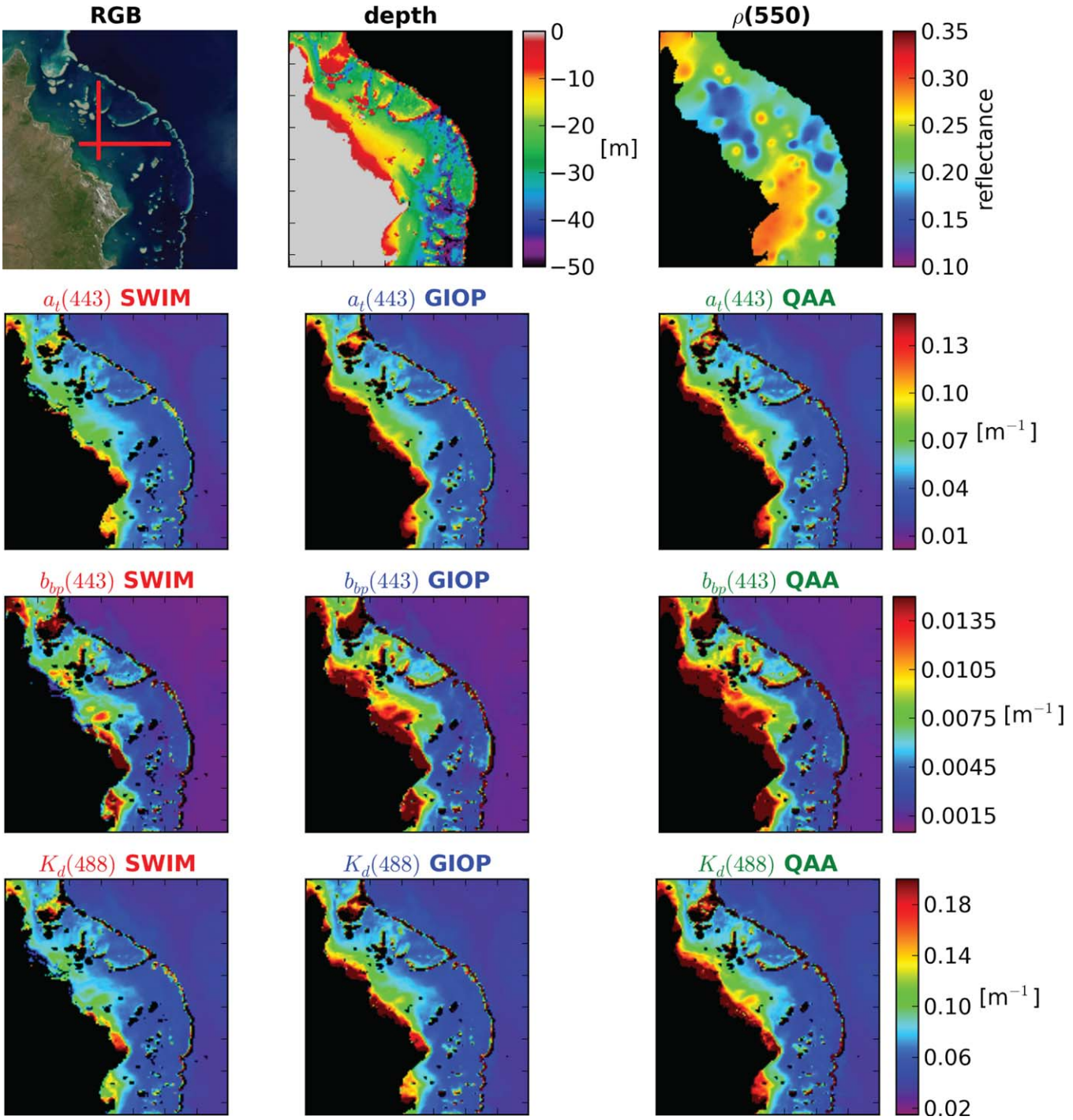

Figure 6. Subset of a MODIS Aqua image swath captured over the northern Great Barrier Reef on 22 May 2009. The top row shows: (i) a RGB true color image in the top left-hand corner with east-west (E-W) and south-north (S-N) transects indicated as red lines, (ii) the water column depth, and (iii) the benthic albedo at 550 nm. The second row shows from left to right values of $a_t(443)$ derived using (i) SWIM, (ii) GIOP, and (iii) QAA. The third row shows from left to right values of $b_{bp}(443)$ derived using (i) SWIM, (ii) GIOP, and (iii) QAA. The bottom row shows from left to right values of $K_d(488)$ derived using (i) SWIM, (ii) GIOP, and (iii) QAA.

East-west (E-W) and south-north (S-N) transects, shown as red lines in the "RGB" subplot (Figure 6), each span 62 image pixels, which is approximately a 62 km length. The water column depth along the E-W and S-N transects ranges from 11.6 to 46.0 and 3.3 to 27.9 m respectively, shown as the dotted black lines in Figure 7. The depth of both cross-shelf transects increases smoothly from the nearshore to mid-shelf waters until the outer coral reef matrix is reached. The S-N transect's depth profile crosses a coral reef at

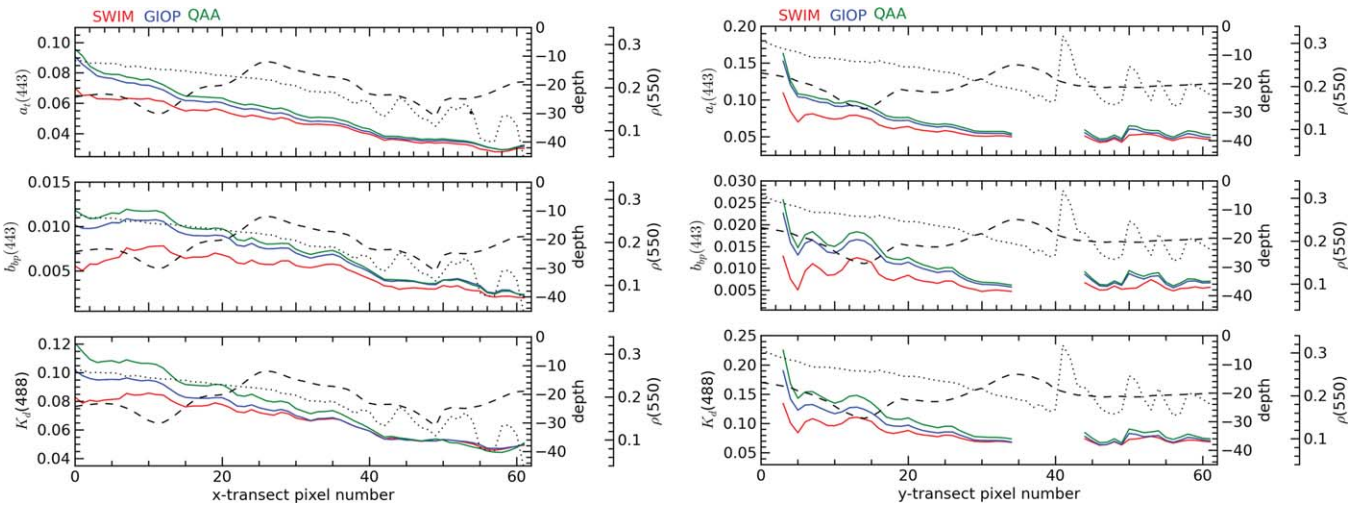

Figure 7. Comparison of $a_t(443)$, $b_{bp}(443)$, and $K_d(488)$ derived using SWIM (red), GIOP (blue), and QAA (green) as cross-shelf water column depth (dotted black) and benthic albedo at 550 nm (dashed black) varies. The location of the (left) east-west (E-W) transect and (right) south-north (S-N) transect are shown in Figure 6. Missing values in the S-N transect were due to straylight contamination that was masked out.

approximately pixel number 40, at which point the depth sharply decreases from 25 to 3 m, then increases to 28 m again after pixel 48. Upon reaching the outer coral reef matrix, undulating bathymetric features become pronounced. Water column depth, $\rho(550)$ and retrieved values of $a_t(443)$ and $b_{bp}(443)$ along the E-W and S-N transects are shown in Figure 7 (left and right), respectively. Whilst differences exist in the magnitudes of $a_t(443)$, $b_{bp}(443)$, and $K_d(488)$ derived using the three different algorithms, a general cross-shelf trend of increasing water clarity is evident in both the E-W and S-N transect plots (Figure 7) as gradual decreases in all IOP values. It should be noted that for the S-N transect, Level-2 quality control flags (see Table 3) were triggered between pixel numbers 34 and 44 resulting in this portion of the transect being masked out (see Figure 7, right). On closer inspection of the level-2 quality flags, we determined that product failures (PRODFAIL) and straylight (STRAYLIGHT) occurred at the edge of a coral reef structure where the water column depth rapidly decreased to become shallower than 5 m. At depths less than 5 m, we hypothesize that straylight from inter-tidal reef crests, sand cays, and wave breaks may contaminate the water-leaving signal within a MODIS Aqua 1 km × 1 km pixel. We thus recommend that SWIM product retrievals in waters shallower than 5 m should be excluded. Further discussion of SWIM product failure is given in Appendix C.

For both the E-W and S-N transects, the SWIM-derived $a_t(443)$, values were consistently lower than those derived using GIOP/QAA when the water column depth is shallower than 30 m. However, as the transect progresses toward the edge of the shelf and the water column depth exceeds 30 m, SWIM-derived values of $a_t(443)$, converge to be of similar magnitude to those derived from GIOP/QAA. These results are consistent with those of the radiative transfer modeling study. Differences between IOPs derived by SWIM and those of GIOP/QAA monotonically decrease with increasing water column depth; this is demonstrated in Figure 8. However, Figure 8 shows that for the E-W and S-N transects, SWIM-derived $a_t(443)$, values remain approximately 0.005 m^{-1} smaller than GIOP and QAA-derived values once the water column exceeds 25 m. The results also show that SWIM-derived values of $b_{bp}(443)$ remain lower than GIOP and QAA-derived values throughout the E-W and S-N transects. Further, once the water column depth exceeds 25–30 m, SWIM-derived values of $b_{bp}(443)$ converge toward GIOP and QAA-derived but remain approximately 0.001–0.003 m^{-1} lower.

For the results shown in Figure 7, $K_d(488)$ values were derived using the IOP-centered approach of *Lee et al.* [2005] using $a_t(488)$ and $b_{bp}(488)$ derived by either SWIM, GIOP, or QAA. As with $a_t(443)$ and $b_{bp}(443)$, SWIM-derived $K_d(488)$ values for both the E-W and S-N transects were smaller than those derived by GIOP and QAA when the water column is less than 25 m deep. The difference between GIOP and SWIM and QAA and SWIM-derived values of $K_d(488)$ monotonically decreases toward zero as water column depth increases (Figure 8). This behavior is expected as any biases in the retrieved bulk IOPs will propagate through to derived $K_d(488)$ values.

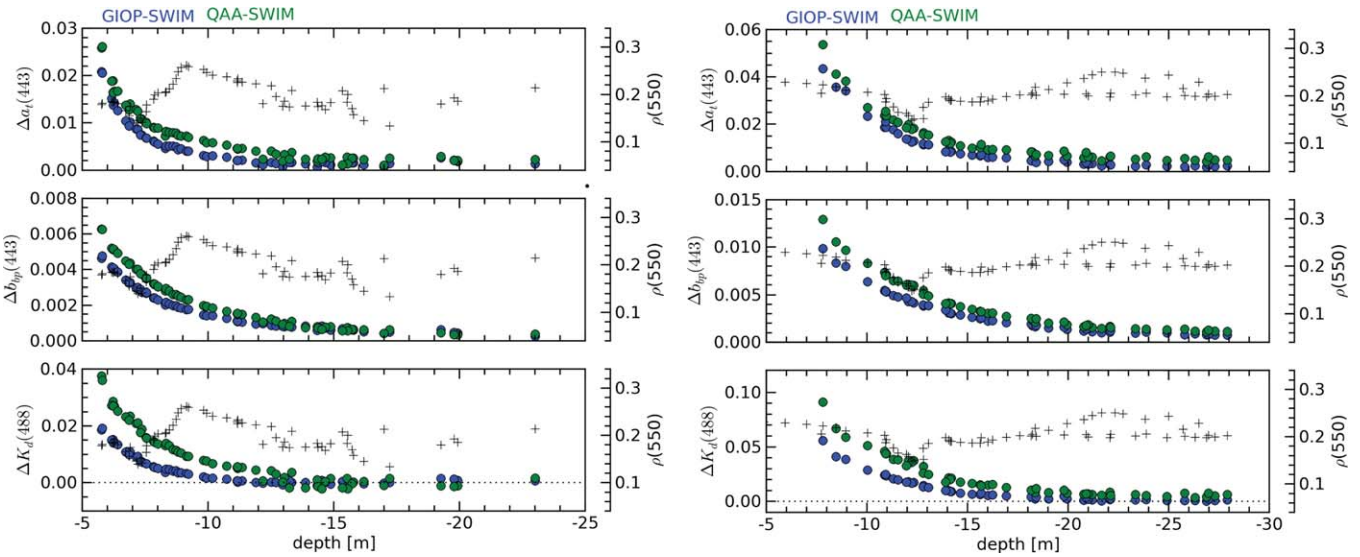

Figure 8. Differences (Δ) between $a_t(443)$, $b_{bp}(443)$, and $K_d(488)$ products derived using: (i) GIOP (blue) and (ii) QAA (green) and those same products derived using SWIM. These differences are plotted against water column depth. Black "plus" symbols show how $\rho(550)$ varies with depth. The data were extracted along the (left) east-west (E-W) and (right) south-north (S-N) transects in Figure 6.

3.2.2. Effect of Depth and Benthic Albedo

Transect plots in Figure 7 demonstrate that cross-shelf differences exist between SWIM-derived products and those of GIOP and QAA, which exhibit a prominent dependence on water column depth, with lesser dependence on benthic albedo. Figure 8 further demonstrates differences between GIOP/QAA and SWIM varying with depth. Notably, Figure 8 shows that along-transect differences in IOPs were highly correlated with depth and less dependent on benthic brightness. It is clear that after the water column depth exceeds 30 m, SWIM provides retrievals very similar to those of GIOP and QAA. Hence, we infer that under the optical conditions of that day (22 May 2009), the influences of both water column depth and benthic reflectance upon the water-leaving signal were diminished, thus the water became quasi-optically deep once the depth exceeded 30 m. The transect results also agree with the general trends of previous modeling studies [*Hochberg et al*., 2003; *Maritorena et al*., 1994] where it was demonstrated that the influence of benthic reflectance upon the net $r_{rs}(\lambda)$ signal monotonically decreases and tends to zero after approximately 10–20 m. However, in the modeling by *Hochberg et al*. [2003], a brown coral albedo was used ($\rho(550) \approx 0.10$) which is typically darker than the benthic reflectance across the test region shown in Figure 6.

It should be clearly noted that the effect of benthic reflectance on $r_{rs}(\lambda)$ is a function of both the optical depth and the brightness of the benthos. That is to say, very clear shallow waters with a bright sandy bottom will influence $r_{rs}(\lambda)$ more so than turbid waters of the same depth with the same sandy bottom. Hence, the "optically deep" limit of 30 m identified in the transect analysis (Figure 8) should not be treated as a "rule of thumb" depth limit at which benthic reflectance effects in the GBR become negligible. Whilst previous studies [*Hedley et al*., 2012; *Hochberg et al*., 2003] have utilized radiative transfer modeling to study and quantify this effect in optically shallow waters, they have focused primarily on detectability limits for classification of benthic types. Thus, for ocean color applications, further examination regarding the influence that differing water column depths, benthic types, and IOPs have upon $r_{rs}(\lambda)$ and ultimately algorithmically-derived IOPs is warranted.

3.3. Time Series Data

The time series analysis allowed for a thorough comparison of the SWIM algorithm's behavior relative to GIOP and QAA. Monthly averaged time series plots of $a_t(443)$, $b_{bp}(443)$, and $K_d(488)$ values derived using SWIM (red), GIOP (blue), and QAA (green) for the DW, LI, and MS regions are shown in Figures 9, 10, and 11 (left), respectively. Figures 9–11 (right) show the relative differences between $a_t(443)$, $b_{bp}(443)$, and $K_d(488)$ values derived using GIOP (blue) and SWIM, and QAA (green) and SWIM for the DW, LI, and NS regions. To quantitatively summarize these plots, monthly data for the DW, LI, and NS regions were condensed into

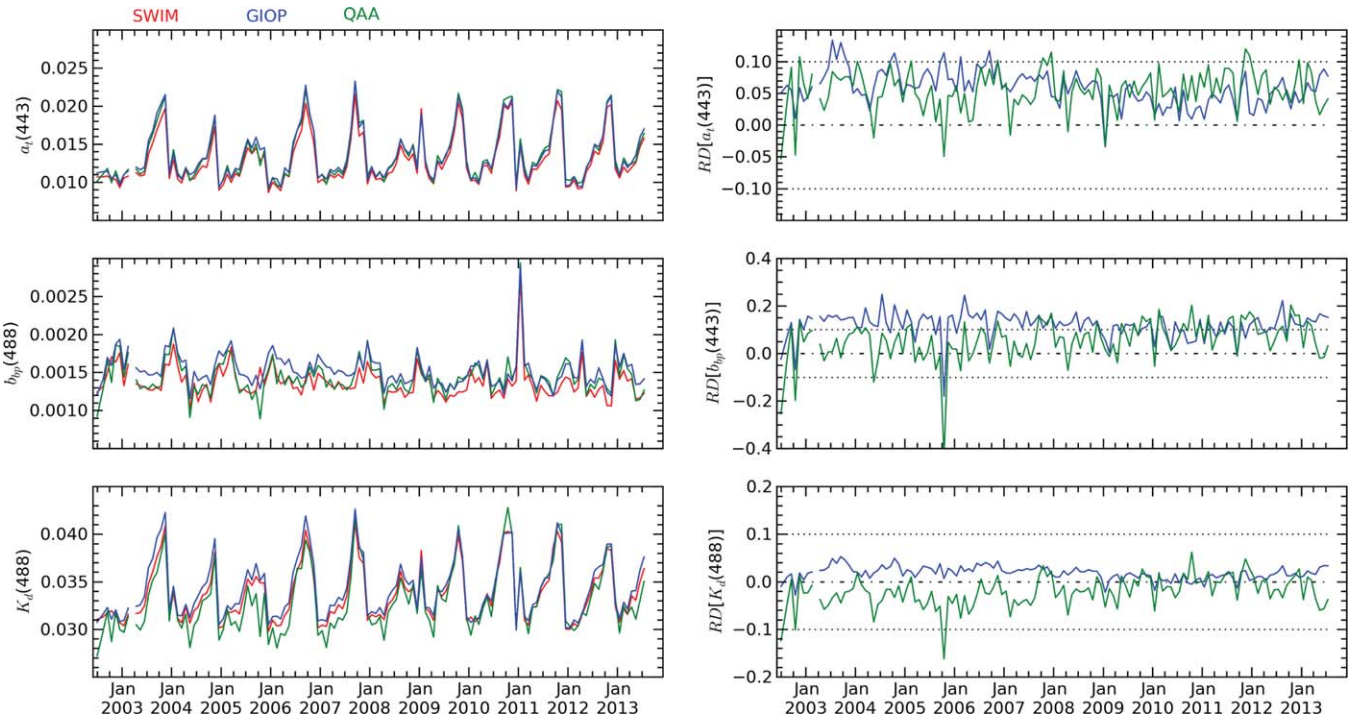

Figure 9. (left) Monthly weighted means of $a_t(443)$, $b_{bp}(443)$, and $K_d(488)$ for the Deep Water (DW) region retrieved using SWIM (red), GIOP (blue), and QAA (green). (right) Relative differences between $a_t(443)$, $b_{bp}(443)$, and $K_d(488)$ values derived using GIOP (blue) and QAA (green) and values derived using SWIM.

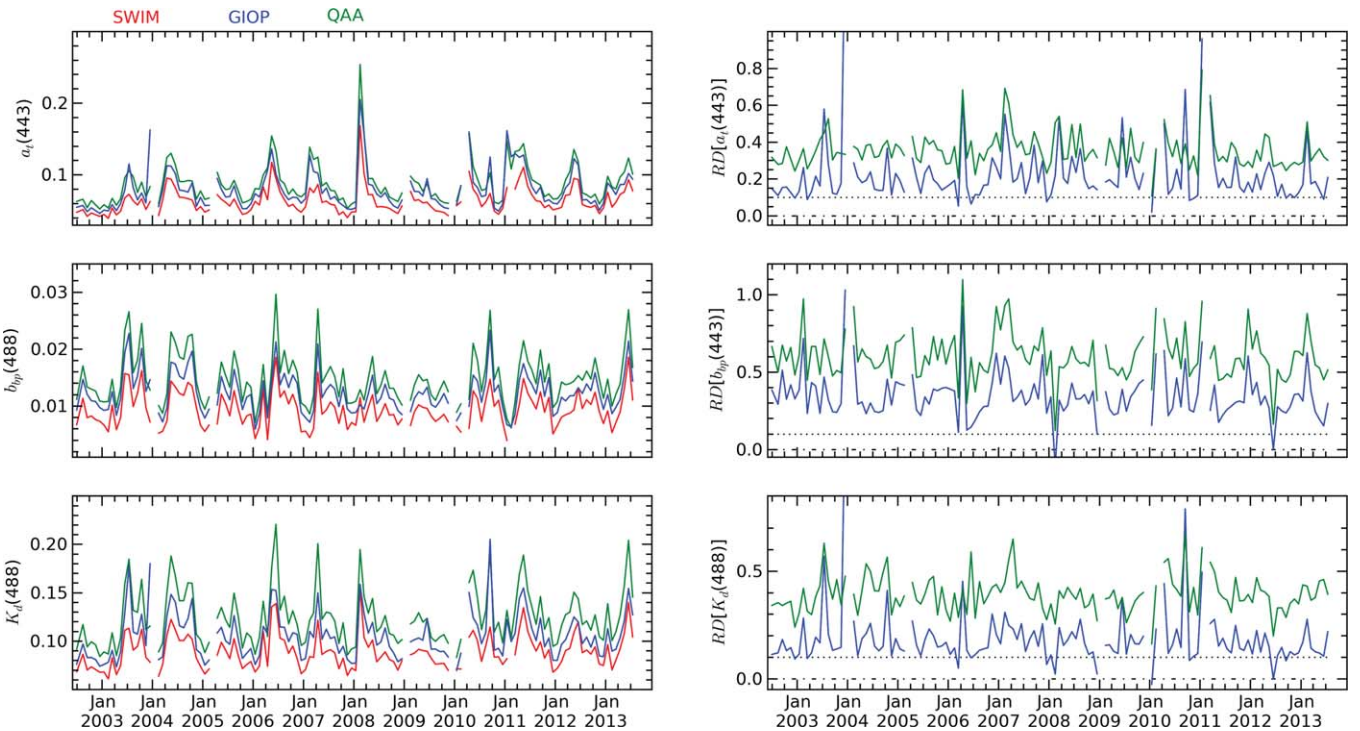

Figure 10. (left) Monthly weighted means of $a_t(443)$, $b_{bp}(443)$, and $K_d(488)$ for the Lizard Island (LI) region retrieved using SWIM (red), GIOP (blue), and QAA (green). (right) Relative differences between $a_t(443)$, $b_{bp}(443)$, and $K_d(488)$ values derived using GIOP (blue) and QAA (green) and values derived using SWIM.

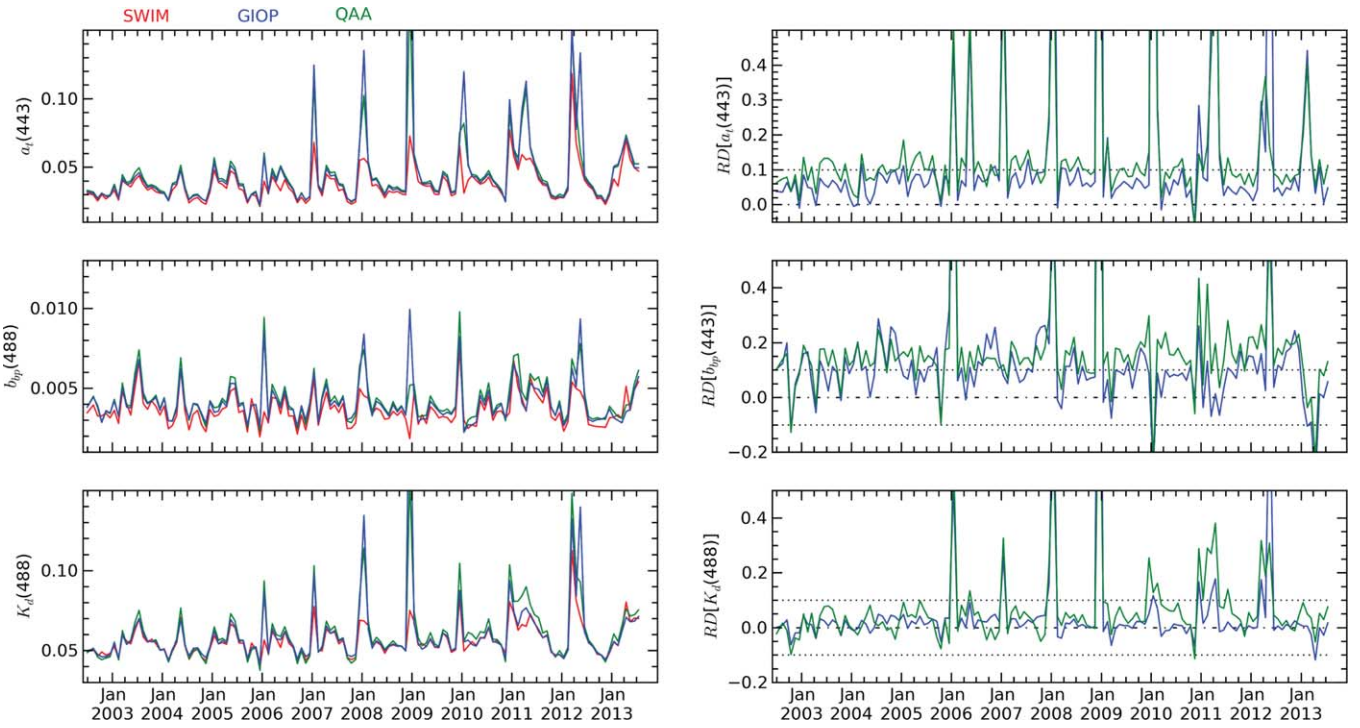

Figure 11. (left) Monthly weighted means of $a_t(443)$, $b_{bp}(443)$, and $K_d(488)$ for the Mid-Shelf (MS) region retrieved using SWIM (red), GIOP (blue), and QAA (green). (right) Relative differences between $a_t(443)$, $b_{bp}(443)$, and $K_d(488)$ values derived using GIOP (blue) and QAA (green) and values derived using SWIM.

seasonal statistics which can be found in supporting information Tables ts05–ts07, respectively. In addition, Taylor [*Taylor*, 2001] and Target [*Jolliff et al*., 2009] summary plots were produced using monthly binned data in order to better understand pattern statistics and biases of GIOP/QAA relative to SWIM across all four test regions (see Figure 12).

3.3.1. Deep Water Region

The Figure 9 (left) shows that for the DW region, SWIM-derived $a_t(443)$, $b_{bp}(443)$, and $K_d(488)$ were very similar to those derived by GIOP and QAA. The relative difference plot (Figure 9, right) indicates that the monthly GIOP and QAA-derived $a_t(443)$ were on average no more than 10% larger than SWIM values. GIOP and QAA-derived $b_{bp}(443)$ values were on average approximately 9% and 4% larger than SWIM values, respectively. When considering $K_d(488)$ values, GIOP values were on average only about 1–2% larger than SWIM-derived values. Interestingly, between the years 2003–2008 QAA values were approximately 1–5% less than SWIM-derived $K_d(488)$ values.

The Taylor diagrams (top row in Figure 12, DW results displayed as circles) confirmed that GIOP/QAA-derived $a_t(443)$ values were very similar in both temporal phase and variability compared to those derived by SWIM, evidenced by high correlations (≈0.99) and normalized standard deviations close to 1.0. The Taylor plots also showed GIOP-derived $K_d(488)$ values were very similar to SWIM values, supporting time series observations. QAA-derived $b_{bp}(443)$ and $K_d(488)$ were less similar to those of SWIM, evidenced by lower correlations (≈0.85 and 0.95) and normalized standard deviations slightly higher than 1.0. The Target plots (bottom row of Figure 12) demonstrated that for the DW region, both GIOP and QAA-derived $a_t(443)$, $b_{bp}(443)$ and $K_d(488)$ were in good agreement with those of SWIM, evidenced by normalized biases and unbiased root mean squared differences (uRMSD) that were less than 1.0. Based on *Jolliff et al*. [2009], we considered Target plot data points that fell outside a radius of 1.0 from the origin (depicted as black circles, bottom row of Figure 12) as points that did not suitably agree with SWIM. We hence refer to the area encompassed by a circle of radius = 1.0 about the origin in a Target plot as the "performance marker region."

As the water column depth, H, increases, the influence of shallow substrate reflectance components (second and third terms in equation (10)) in the shallow water model decrease relative to the contribution of

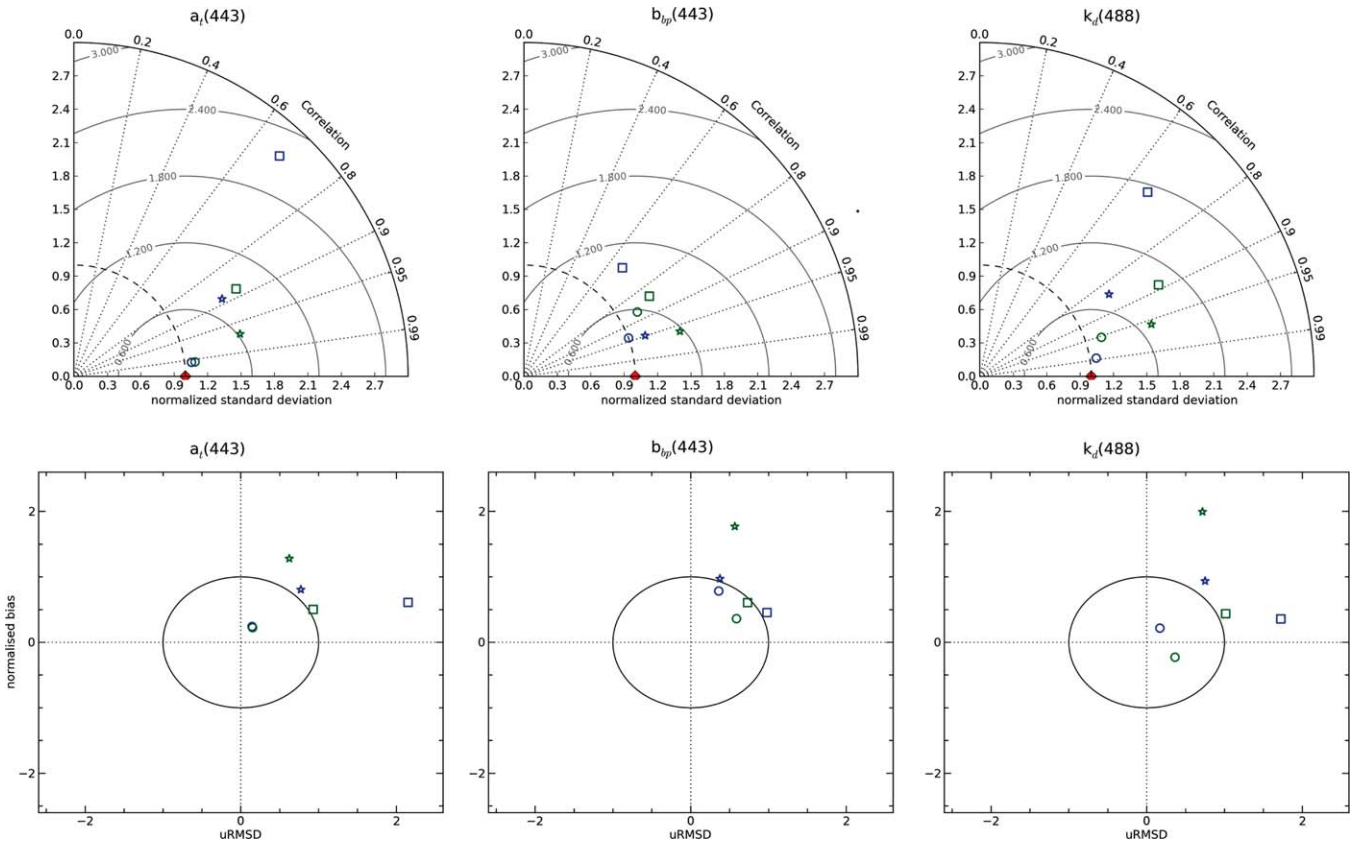

Figure 12. (top row) Taylor and (bottom row) Target diagrams of GIOP/QAA relative to SWIM (red points) using monthly binned MODIS time series data. The three columns (left-to-right) represent $a_t(443)$, $b_{bp}(443)$, and $K_d(488)$, respectively. Symbol shapes represent each test region as follows: circle = DW, star = LI, and square = MS. Symbol colors represent the following: blue = GIOP, green = QAA, and red = reference.

the deep water reflectance (first term in equation (10)). Therefore, in the Deep Water (DW) region where the water column depth far exceeds the optical depth, SWIM mathematically transitions into an optically deep SAA of similar structure to that of GIOP. Initially, it was expected that SWIM-derived IOP values would converge very closely toward those of GIOP/QAA, yet analysis of the time series revealed that GIOP and QAA retrievals of IOPs were on average about 5–10% larger than those of SWIM ($\pm$10% level is represented by dotted lines in Figure 9). However, these relative differences in $a_t(443)$ and $b_{bp}(443)$ equate to small absolute values in the order of 0.001 and 0.0001 m^{-1}, respectively, and are consistent with results of the radiative transfer study. In addition, the time series analysis showed that SWIM-derived $K_d(488)$ values were very similar to those of GIOP/QAA. These results were also consistent with the radiative transfer modeling case study (section 3.1) which indicated that SWIM, GIOP, and QAA have good precision and negligible bias in optically deep water. A more concerning observation, however, was that the number of valid pixels derived by SWIM were approximately 25% less per annum than those of GIOP/QAA (supporting information Tables ts05–ts07). This result suggested that SWIM converged to a solution on average 25% less of the time than GIOP/QAA.

The radiative transfer modeling study using synthesized IOP data showed GIOP and QAA-derived IOPs had slightly positive mean biases relative to actual values, whereas SWIM results had slightly smaller mean biases (Table 5). Analysis of the time series show that relative to SWIM, GIOP, and QAA-derived values for the DW region had slightly positive bias, typically less than 10%. In the DW region, we expected SWIM, GIOP, and QAA to be very similar and we hypothesize that the small relative differences observed are likely due to differences in each algorithm's internal IOP parameterization. In order to assist visual interpretation of the relative difference plots, horizontal dotted lines at $\pm$10% were included (Figures 9–11, right). Relative differences greater than this 10% threshold were deemed likely to be significant. In addition, the Taylor and Target plots (Figure 12) were used as a supplementary method for discerning significant differences.

Relative differences in retrieved IOPs for the DW region seemed greatest from 2003 to 2008. Most noticeably, QAA-derived $K_d(488)$ values were approximately 2–5% less than those of SWIM for 2003–2008. However, these differences became minimal from 2008 to 2013 (Figure 9). We postulate that during 2003–2008, differences in derived values were due to different IOP spectral shape parameterizations within SWIM, GIOP, and QAA. For example, within default parameterization of GIOP, the spectral slope coefficients of $a_{dg}(\lambda)$, S, is 0.018 whereas for SWIM, S was set to 0.017. For the QAA, a band ratio approach is used to parameterize S. Further, the power law coefficient for $b_{bp}(\lambda)$, γ, used in SWIM is 1.0 whilst for GIOP and QAA a band ratio approach is implemented to estimate γ. Also, within SWIM, $a^*_\phi(\lambda)$ was parameterized by using a single region-specific normalized spectral shape. However, for GIOP, the default spectral shape of $a_\phi(\lambda)$ can vary pixel-by-pixel using spectral data from *Bricaud et al.* [1998] combined with a forward estimate of CHL concentration derived using the OC3 band ratio algorithm [*O'Reilly et al.*, 1998]. Finally, the QAA approach, unlike SWIM and GIOP, does not use a spectral model for $a_\phi(\lambda)$. Instead, QAA calculates $a_\phi(\lambda)$ in its final processing step by subtracting $a_w(\lambda)$ and $a_{dg}(\lambda)$ from the derived value of $a(\lambda)$.

It has been demonstrated that use of different S and γ values and a single fixed $a^*_\phi(\lambda)$ shape can indeed affect derived IOPs [*Werdell et al.*, 2013a]. The ability to dynamically vary these parameters within an inversion algorithm may be advantageous for environments such as the GBR where the optical properties of the water column are complex both temporally and spatially. Within GIOP and QAA, spectral IOP models are dynamically varied using band ratio empirical models thereby allowing the algorithms to adapt to subtle changes in optical water types [*Lee et al.*, 2002; *Werdell et al.*, 2013a]. However, in optically shallow regions, the use of band ratio algorithms may be hampered by variations in benthic reflectance, which may lead to erroneous product retrievals. As an alternative to a band ratio approach, *Brando et al.* [2012] demonstrated a method in which region-specific IOP spectral shapes can be adaptively varied within a semianalytical inversion algorithm based on the optical water types being observed.

3.3.2. Lizard Island Region

The time series plots (Figure 10) for the LI region indicated the relative difference between GIOP and QAA-derived $a_t(443)$, $b_{bp}(443)$ and $K_d(488)$ values and those of SWIM mostly exceeded 10%. The Taylor plots (Figure 12) showed that GIOP-derived $a_t(443)$, $b_{bp}(443)$, and $K_d(488)$ values relative to SWIM had high correlations (0.8–0.95) and normalized standard deviations ranging between 1.15 and 1.5, whereas QAA relative to SWIM had high correlations ($\approx$0.95) and normalized standard deviations of 1.6–1.7. These results indicated both GIOP and QAA were temporally in phase with SWIM but had slightly higher variability. From examining the Target plots (Figure 12), we noted that QAA and GIOP had normalized biases greater than 1.0, and thus fell outside the performance marker region. We therefore conclude that for the LI region, GIOP and QAA typically overestimated $a_t(443)$, $b_{bp}(443)$, and $K_d(488)$ values relative to SWIM, a finding that agrees with the transect plots of the same region discussed earlier (section 3.2) and the radiative transfer modeling study.

We note that for the LI region, whilst the number of valid pixels for SWIM was less than GIOP/QAA, the relative number was higher for LI than the other two test regions. Specifically, SWIM has 5–6 % fewer valid pixels that GIOP/QAA during the winter/spring, 15% fewer during summer/autumn, and annually 8% fewer. These results indicate that the SWIM algorithm tended to converge to a solution more often for LI than the other two regions. We hypothesize that this is either because: (i) the spectral IOP models within SWIM are well suited to this region, and/or (ii) the LI region is not subject to frequent river flood plume events for extended periods that disperse sediment plumes and/or highly attenuating water [*Petus et al.*, 2014] that may cause product failure.

These results indicate that GIOP and QAA-derived values of $a_t(443)$, $b_{bp}(443)$, and $K_d(488)$ were indeed larger than those derived by SWIM but were temporally in phase with good correlation. This result was expected and is attributed to the optically shallow nature of the LI region. In particular, we expected benthic albedo effects to be compensated for within the optically deep models by overestimating $b_{bp}(443)$ as demonstrated within the radiative transfer modeling study. Interestingly, GIOP retrievals were found to be more similar to SWIM than QAA retrievals. This was not surprising considering both GIOP and SWIM have similar forward-inverse optimization-style structures, whereas QAA solves for IOPs algebraically using a series of semiempirical relationships. In particular, QAA is initialized using a band-ratio method to estimate total absorption, $a(\lambda_0)$, at a reference wavelength, λ_0, [*Lee et al.*, 2002]. For MODIS, QAA typically sets λ_0 to 547 nm—a spectral region which is most influenced by benthic albedo [*Barnes et al.*, 2013]. Thus, any contamination from benthic albedo that occurs at 547 nm is likely propagated through the QAA to the resultant

IOPs. These findings support work by *Barnes et al*. [2013] in which the QAA was adapted by setting λ_0 to 667 nm, a region deemed less susceptible to benthic albedo contamination. The result of shifting λ_0 resulted in improved $K_d(488)$ retrievals when using the *Lee et al*. [2005] IOP-centered approach.

3.3.3. Mid-Shelf Region

For the MS region, GIOP and QAA-derived $a_t(443)$, $b_{bp}(443)$ and $K_d(488)$ were consistently within 10% of values derived using SWIM (Figure 11) except for annual periodic events, evident as sharp spikes in the time series, that occurred in the summer/autumn between 2007 and 2012. During these annual events, GIOP and QAA-derived values were between 50 and 400% larger than those of SWIM. Because of the average water column depth of the MS region (44 m), we initially infer that the benthic effect here is small and hence SWIM should perform in a similar manner to GIOP and QAA.

The Taylor plots in Figure 12 demonstrate that relative to SWIM, GIOP-derived $a_t(443)$, $b_{bp}(443)$, and $K_d(488)$ values had high variability and low correlation coefficients of approximately 0.65. Relative to SWIM, QAA-derived $a_t(443)$, $b_{bp}(443)$ and $K_d(488)$ values had high variability and correlation coefficients of 0.90, 0.81, and 0.90, respectively. This suggests that for the MS region, GIOP and QAA-derived values had higher variability and were less temporally in phase with SWIM-derived values. Further, using the Target plots, we were able to discern that the normalized biases and uRMSD for GIOP relative to SWIM were in excess of 1.0 for $a_t(443)$, $b_{bp}(443)$ and $K_d(488)$ with all data points lying outside the performance marker region. The Target plots also indicate that QAA-derived $a_t(443)$ and $K_d(488)$ were different from SWIM, however, QAA-derived $b_{bp}(443)$ values fell just inside the performance marker region. Based on the relative difference plots and the Taylor and Target diagrams, we could infer that GIOP and QAA-retrieved values were mostly different from SWIM values for the MS location. However, these results should be interpreted with caution, particularly because SWIM had distinctly less valid pixels than GIOP and QAA during summer/autumn (supporting information Table ts07), an effect that is not clear from interpreting the Taylor and Target plots alone.

We concede it is a challenge applying ocean color remote sensing algorithms in the MS region as it is moderately shallow, optically complex, and is subject to abrupt changes in optical regimes driven by events such as river flood plumes [*Devlin et al*., 2012], wind-driven sediment suspension events [*Orpin and Ridd*, 2012] and intrusions of clear oceanic water [*Choukroun et al*., 2010]. We assumed the QAA algorithm might perform relatively well under such variable conditions [*Qin et al*., 2007] and noted that GIOP agreed well with the QAA throughout the MS time series. We also note that SWIM-derived values were mostly within 10% of GIOP and QAA except through 2007–2012 for which large spikes in GIOP/QAA-derived IOPs occurred during the austral summer/autumn. During these events, GIOP and QAA-derived values were up to 400% larger than those of SWIM. However, during summer/autumn, SWIM retrieved on average 23% less valid pixels than GIOP or QAA. These observations suggest that the default parameterization of SWIM was unable to retrieve IOPs with the same dynamic capability as GIOP and QAA particularly during turbid, optically complex conditions for which the impact of substrate reflectance would be reduced. As this is a comparative study, we cannot conclusively comment on the whether SWIM was more or less accurate than GIOP/QAA for the MS region. However, we infer that the spectral IOP models within SWIM are presently not robust during turbid, optically complex events resulting in product failure and hence less valid pixels relative to GIOP/QAA.

3.3.4. Seasonal Variability

Interpretation of seasonal variability in the LI and MS regions indicated that clearest optical conditions occur each austral spring (September, October, November) with the least clear conditions occurring in the Austral summer/autumn (December to May). This is consistent with *Weeks et al*. [2012] who used a regionally tuned water clarity algorithm to determine that clearest waters in the central and southern GBR occur during September due to strong intrusions onto the GBR shelf of clear oligotrophic waters from the Coral Sea. *Weeks et al*. [2012] also reported that least clear optical conditions occur during the Austral Wet Season (summer-autumn), during which high rainfall events cause riverine discharge of terrestrial nutrients and sediments that flow onto the GBR shelf [*Brodie et al*., 2012; *Devlin et al*., 2012].

An annual wet season/monsoon signal was observed within the LI and MS time series plots (Figures 10 and 11) as distinct spikes occurring during the austral summer-autumn. These quasi-annual spikes in IOPs coincide with high rainfall events that occurred during the annual monsoon season, resulting in high river flow events that discharge buoyant freshwater plumes [*Devlin et al*., 2012; *Schroeder et al*., 2012]. For the MS

region, spikes in the IOP time series relate particularly well with the monthly discharge data (river discharge data available from Queensland State Government: http://watermonitoring.derm.qld.gov.au/host.htm) from the nearby Burdekin River (results not shown), which is in agreement with previous studies of flood plume extent and duration [*Fabricius et al*., 2014; *Petus et al*., 2014; *Schroeder et al*., 2012]. Such freshwater plumes can deliver sediment laden water, elevated CDOM, and nutrients that can lead to increased phytoplankton growth. Thus, we conclude that during highly turbid events such as river flood plumes, SWIM is less able to converge to a solution, resulting in fewer valid pixels, and average monthly IOP retrievals that were biased low relative to GIOP and QAA.

3.4. Shallow Water Retrieval Overview

Within the time series comparisons, we did not expect nor did we observe, SWIM-retrieved values to be temporally out of phase with GIOP/QAA-derived values in the optically shallow test region, LI. This was evidenced by good correlations in the Taylor plots (Figure 12). We did however observe that GIOP/QAA retrievals were biased high relative to SWIM, supporting established concerns that benthic reflectance in optically shallow waters leads to overestimations of IOPs by GIOP/QAA. Specifically for the LI region, mean annual GIOP-derived values relative to those of SWIM were biased high by 13% for $a_t(443)$, 31% for $b_{bp}(443)$, and 17% for $K_d(488)$. Similarly for the LI region, mean annual QAA-derived values were biased high relative to those of SWIM by 25% for $a_t(443)$, 56% for $b_{bp}(443)$, and 38% for $K_d(488)$. Encouragingly, the relative differences observed between GIOP/QAA and SWIM in the MODIS Aqua time series for the LI region are in agreement with those determined from radiative transfer modeling (section 3.1). Thus, we can stipulate with greater confidence that the differences observed between SWIM and GIOP/QAA for the LI region were due to water column depth and benthic albedo effects. Overall, the results from both radiative transfer modeling and MODIS Aqua time series analysis indicate that the SWIM algorithm is performing as expected.

Whilst we have demonstrated the feasibility of implementing an optically shallow ocean color inversion algorithm using radiative transfer modeling and ocean color time series data, it is difficult to comment further on the absolute accuracy of the SWIM algorithm without available in situ IOP matchup data. At the time of writing this paper, in situ IOP data collected in the GBR by the Australian Commonwealth Scientific and Industrial Research Organization (CSIRO) between 2002 and 2005 [*Blondeau-Patissier et al*., 2009] were in the process of being loaded onto the publicly accessible Integrated Marine Observing System (IMOS) Australian Ocean Data Network (AODN) portal (http://imos.aodn.org.au/imos123/). Once available, essential validation of SWIM-derived IOPs can be performed and published in the literature. Consequently, for this research, we were limited to performing radiative transfer modeling and relative comparisons between algorithms using the MODIS Aqua time series data. Another potential source of in situ IOP validation data for the Great Barrier Reef region is the IMOS Lucinda Jetty Coastal Observatory (LJCO), commissioned on 28 October 2009 (http://imos.org.au/ljco.html). The LJCO IOP data are currently in the process of being distributed and should be available through the IMOS AODN in the near future.

In lieu of in situ IOP matchup data, we are still able to anecdotally comment on whether the magnitude of SWIM-derived IOPs are realistic based upon IOP summaries published by *Blondeau-Patissier et al*. [2009], hereby referred to as BP2009. To facilitate a crude comparison, we have made a broad assumption that the optical regimes of the LI region are analogous to "Reef Waters" sampled by BP009. Similarly, we assume the MS region analogous to the BP2009's "Townsville" region. Sampling of the "Townsville" and "Reef Waters" regions by BP2009 occurred during the Australian Dry Season. Consequently, we chose to compare average SWIM-derived $a_t(443)$ and $b_{bp}(443)$ values for the Austral spring with those of BP2009. Note, BP2009 reported only the measured ranges of $b_{bp}(555)$. In order to estimate measured values of $b_{bp}(443)$, for comparison with SWIM, we have scaled values of $b_{bp}(555)$ using power law functions (equation (6)). The power law functions were parameterized with $\gamma = 1.701$ and $\gamma = 0.655$ as reported by BP2009 for the "Reef Waters" and "Townsville" regions, respectively.

The comparison (results not shown) indicated that spring-averaged IOPs derived by SWIM fell within the range of IOPs measured in the "Dry Season" by BP2009. This comparison gives us a rudimentary indication that SWIM is deriving IOPs within a realistic range for the GBR; however, we concede that spring-averaged GIOP and QAA-derived IOPs also fall within the range measured by BP2009. However, our radiative transfer modeling gives us confidence that SWIM-derived IOPs would be more realistic than those of GIOP and QAA

in optically shallow waters. Nonetheless, we reiterate the need for comprehensive validation of the SWIM algorithm once in situ data become available through the IMOS AODN.

3.5. Product Failure

Our study of the three test regions indicated that SWIM consistently had fewer valid pixels than GIOP and QAA. On closer investigation, we conclude that for certain pixels SWIM was unable to converge to a solution (i.e., reduce the cost function below the predefined threshold) within the maximum number of predefined L-M iterations; an outcome which seemed to occur more often during turbid, optically complex events and often adjacent to cloud edges (results not shown). By this reasoning, one might expect that the number of valid SWIM-derived pixels for the DW region (nonoptically complex waters) should have been of similar magnitude to those of GIOP and QAA, not 25% less. We therefore cannot attribute product failure solely to turbidity plumes or cloud edges. We hypothesize that that the consistently reduced number of valid SWIM-derived pixels may also be due to: (i) the spectral IOP models used within SWIM being fixed in shape, (ii) the convergence criteria and/or the boundary constraints used in the L-M routine being overly strict, or, (iii) variability in water column depth due to tidal cycles not being parameterized within SWIM.

In Appendix C, we briefly demonstrate the effect of varying the spectral slope of $a_{dg}(\lambda)$, S, and the power exponent of $b_{bp}(\lambda)$, γ, on the number of product failures in a test scene of the far northern Great Barrier Reef. These results indicate that varying S and γ can indeed increase the number of valid pixels by up to 20% (Table C1) and thus lends merit to the concept of dynamically varying IOP spectral models rather than leaving them fixed. As mentioned previously, both GIOP and QAA have the ability to vary the spectral shapes of internal IOP models, thus we suggest GIOP and QAA are likely to give more valid retrievals than SWIM. However, this does not necessarily guarantee the correctness of IOPs retrieved by GIOP and QAA. More specifically, both GIOP and QAA dynamically adjust internal IOP spectral shapes using band ratio algorithms. Such band ratio relationships are likely to be confounded by benthic reflectance in optically shallow waters, and propagate through the algorithm leading to potentially erroneous IOP retrievals.

It should be noted that within this study, we have not included tidal cycle offsets to the absolute water column depth used by SWIM. This is certainly likely to have consequences in nearshore and other very shallow regions ($<$10 m) of the GBR where the magnitude of the tidal range is typically 2–3 m, but can be as much as 8–10 m for regions in the southern GBR, such as Broad Sound. We therefore conclude that SWIM's present inability to characterize tidal offsets, which may be of similar magnitude to the water column depth, might also be a cause of product failure in the shallow nearshore zone where PRODFAIL flags were observed (results not shown). A feasible approach to remedy this would be to integrate a tide predictive model into the SWIM algorithm. One suitable method may be the Oregon State University's Tidal Predictive Software (OTPS) [*Egbert and Erofeeva*, 2002], which is able to calculate region-scale tidal solutions with computational efficiencies that may be suitable for pixel-by-pixel retrievals.

4. Concluding Remarks

We have described and demonstrated a semianalytical inversion algorithm for optically shallow ocean color applications: the Shallow Water Inversion Model (SWIM). SWIM has the potential to improve ocean color retrievals of IOPs and subsequent downstream IOP-centered products such as CHL, SPM, the diffuse attenuation coefficient of photosynthetically active radiation ($K_d(PAR)$), and the euphotic zone depth (Z_{eu}). Thus, new and highly significant ocean color time series data may be provided by SWIM that will lead to improved understanding of trends and variability of water quality in sensitive shallow water ecosystems such as seagrass meadows and coral reefs.

By examining the MODIS Aqua time series, we determined that the current SWIM algorithm's default IOP model parameterizations were sufficient for clear coral reef waters of the GBR region. However, during turbid, optically complex events SWIM had difficulty converging to a solution, evidenced by a reduced number of valid pixels relative to GIOP and QAA. This suggests that the fixed spectral IOP shapes used within SWIM are not robust for optically complex mid-shelf and nearshore waters. We propose this limitation can be

remedied by allowing the spectral IOP model shapes to dynamically vary on a pixel-by-pixel basis, however, further research is required to develop a mechanism for doing so. For optically deep waters, algorithms such as the GIOP and QAA rely on empirical band ratio relationships, an approach which may be confounded in optically shallow waters. Alternatively, the adaptive approach of *Brando et al*. [2012] may be used whereby optical water type classifications are implemented in order to parameterize spectral IOP models within an inversion algorithm.

Within this evaluation of the SWIM algorithm, we have used a two-class benthic albedo map, derived using comprehensive benthic survey data. We concede that using only two spectral albedo types (i.e., "light" and "dark") is unlikely to capture sufficient variability of benthic spectral albedos within the GBR region. As such, work in the form of radiative transfer modeling and *in situ* field sampling is currently underway to determine the optimal number of benthic classes necessary for the benthic spectral albedo data used in SWIM. Special consideration must be given to both the spectral and spatial resolution of the ocean color sensor being used. Here we have demonstrated SWIM's capabilities using multispectral MODIS Aqua imagery. However, application of SWIM to existing sensors with higher spectral resolutions such as the Hyperspectral Imager for the Coastal Ocean (HICO), or those being prepared/planned for launch such as the Ocean and Land Color Instrument (OLCI) aboard ESA's Sentinel-3 mission, and the Ocean Color Imager (OCI) aboard NASA's Pre-Aerosol, Clouds and ocean Ecosystem mission (PACE) [*NASA*, 2012], may necessitate the inclusion of more benthic classes within SWIM.

Another interesting aspect not considered in this research is the effect that benthic slope has upon SWIM. Within SWIM we assume that for each MODIS pixel the seafloor is a homogenously flat Lambertian surface. However, within a 1 km × 1 km pixel, a degree of depth variability and seafloor slope is almost certain. *Mobley and Sundman* [2003] showed that a sloping seafloor can have an effect on water-leaving radiances and it may be possible to correct for a sloping seafloor to a certain extent by adjusting the solar incidence geometry. Investigating both the effect of a sloping seafloor on SWIM-derived products and a subsequent correction scheme is an interesting avenue of future work. If necessary, implementation of a geometric correction scheme seems plausible considering the seafloor slope could be calculated using the 100 m × 100 m resolution 3D-GBR bathymetry data set.

Finally, SWIM has been developed within the versatile SeaDAS L2GEN processing framework which allows the algorithm to be applied not only to MODIS Aqua but also to other ocean color imagery captured by past, present and soon-to-be launched sensors including: SeaWiFS, MERIS, HICO, OLCI, and the Visible Infrared Imaging Radiometer Suite (VIIRS). In addition, future sensors, such as the proposed OCI aboard NASA's planned PACE mission, with high spectral (∼5 nm) resolutions and high signal-to-noise ratios (∼1000) would provide unprecedented quality data for use with SWIM for the purpose of monitoring optically shallow regions. Further, the SWIM algorithm is structured within L2GEN such that it is portable to regions beyond the GBR, such as the Florida Keys. Currently, in lieu of user supplied bathymetry and albedo data sets, the SWIM algorithm within L2GEN defaults to ETOPO-1 global bathymetry [*Amante and Eakins*, 2009] and uses a scene-wide sand albedo spectrum. This may produce suboptimal IOP retrievals and as such, a product warning flag (PRODWARN) is appended to such retrievals. Ideally, an end-user can supply their own region-specific bathymetry and benthic albedo maps in netCDF format with the appropriate file attributes. We therefore believe SWIM will provide significant benefit for/to the GBR region and elsewhere.

Appendix A

To briefly demonstrate the effect optically shallow water has on IOPs derived using an optically deep SAA, we present a simple modeling exercise. Figure A1 shows subsurface remote sensing reflectances, $r_{rs}(\lambda)$, modeled using an optically deep semianalytical model (equation (1), section 2.2.1) as blue lines denoted "DEEP-MOD." Red lines denoted "SWIM-MOD" are $r_{rs}(\lambda)$ values modeled using the optically shallow semianalytical model (equation (10), section 2.3.1). Values of $r_{rs}(\lambda)$ were modeled at four different depths using two optical examples summarized in Table A1. The benthic albedo used in this

Table A1. Inherent Optical Properties of Two Examples Used in the Optically Shallow Modeling Exercise

Optical Example	$a_\phi(443)$ (m^{-1})	$a_{dg}(443)$ (m^{-1})	$b_{bp}(443)$ (m^{-1})
1	0.02	0.05	0.01
2	0.05	0.1	0.025

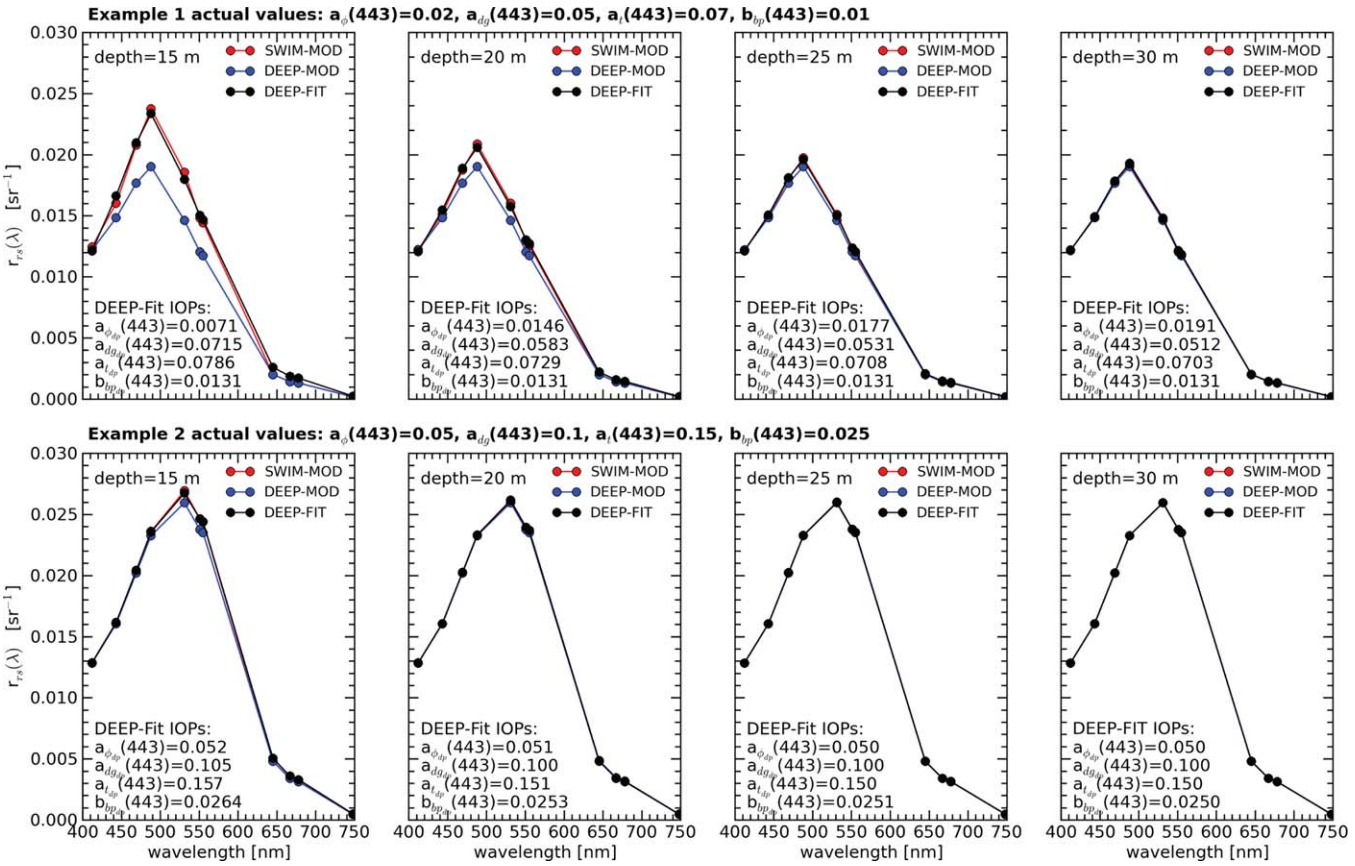

Figure A1. (top and bottom) The effect of depth (varying left-to-right) upon $r_{rs}(\lambda)$ using two different optical scenarios. The red and blue lines denoted "DEEP-MOD" and "SWIM-MOD" are $r_{rs}(\lambda)$ modeled using the *Gordon et al*. [1988] (equation (1)) and *Lee et al*. [1998] (equation (10)) semianalytical forward models, respectively. Values denoted as "DEEP-Fit IOPs" represent IOPs derived from the SWIM-MOD modeled $r_{rs}(\lambda)$ using an inversion algorithm similar to the GIOP algorithm. The black line denoted as "DEEP-FIT" is the $r_{rs}(\lambda)$ reconstructed using the *Gordon et al*. [1988] semianalytical forward model seeded with the DEEP-Fit IOP values.

exercise was constructed of 75% "light" and 25% "dark" substrates (see section 2.3.3). Next, the SWIM-MOD $r_{rs}(\lambda)$ spectra were inverted using an optically deep semianalytical inversion algorithm (similar to GIOP algorithm). These optically deep inverted results are listed in each subplot of Figure A1 as "DEEP-Fit IOPs." Finally, the DEEP-Fit IOPs were passed back to the optically deep forward model (equation (1)) to determine how closely the reconstructed $r_{rs}(\lambda)$, denoted "DEEP-FIT," matched the original SWIM-MOD $r_{rs}(\lambda)$ shallow water spectra.

By examining the first optical example (top four plots of Figure A1), it is evident that the SWIM-MOD $r_{rs}(\lambda)$ spectra are distinctly different from those of DEEP-MOD spectra until the water column reaches 30 m in depth. It is important to note that the DEEP-FIT reconstructed spectra tend to closely match those of SWIM-MOD even when the derived IOPs (listed in Figure A1 as "DEEP-Fit IOPs") are different to those used to simulate SWIM-MOD. This illustrates how an optically deep SAA will converge to a solution (i.e., the modeled $r_{rs}(\lambda)$ spectra match sensor-observed spectra well) whilst retrieving inaccurate IOPs. Examining the second optical example which is slightly more attenuating than the first (bottom plots of Figure A1), we see that SWIM-MOD and DEEP-MOD become extremely similar in shape and magnitude once the water column depth reaches 20 m. In addition, the derived DEEP-Fit IOPs are similar to the true values even when the water column is 15 m deep. This illustrates that, even with the same water column depth and underlying benthic reflectance, the water can be considered optically deep if the water column is suitably attenuating. Thus, we have demonstrated that optically deep algorithms can yield erroneous IOP retrievals in optically shallow waters, supporting the concept of a dedicated optically shallow ocean color algorithm that uses a priori knowledge of water column depth and the benthic albedo.

Table B1. Normalized Phytoplankton Absorption Coefficient Used Within the SWIM Algorithm

Wavelength	412	443	488	531	551	667	678
$a^*_\varphi(\lambda)$	0.840	1.0	0.689	0.217	0.146	0.292	0.356

Appendix B

A region-specific spectral phytoplankton absorption coefficient, $a_\phi(\lambda)$, was used within the SWIM semianalytical inversion algorithm. Seawater samples collected off Heron Reef {3.45°S, 51.95°E} in the southern GBR were filtered, frozen, stored, and analyzed following the Ocean Optics Protocols [*Mitchell et al*., 2002]. Photometric measurements were conducted using a Perkin-Elmer Lambda 35 Spectrophotometer with an integrating sphere attachment following the quantitative filter technique [*Mitchell*, 1990; *Mitchell et al*., 2002]. Values of $a_\phi(\lambda)$ were normalized to 1.0 at 443 nm and are presented below in Table B1.

Table C1. SWIM Product Failures Occurrence for a MODIS Aqua Test Scene Captured on 22 May 2009 as the Coefficients S and γ are Varied

S	γ	PRODFAIL	Relative Difference %
0.010	0.5	37,361	413
0.010	1.0	43,038	491
0.010	1.5	47,945[a]	558
0.015	0.5	8387	15
0.015	1.0	9465	30
0.015	1.5	11,124	53
0.017	0.5	6920	−5
0.017	1.0	7285[b]	—
0.017	1.5	7859	8
0.020	0.5	6024	−17
0.020	1.0	6144	−16
0.020	1.5	6318	−13
0.025	0.5	5719[c]	−22
0.025	1.0	5769	−21
0.025	1.5	5833	−20

[a]Largest increase in product failure.
[b]Standard SWIM parameterization.
[c]Largest reduction in product failure.

Appendix C

The spectral absorption coefficient of colored dissolved and detrital matter, $a_{dg}(\lambda)$, and the particulate backscattering coefficient, $b_{bp}(\lambda)$, can be modeled using exponential and power law functions, respectively [*Bricaud et al*., 1981; *Carder et al*., 1999]. Varying the exponential slope coefficient, S, used to model $a_{dg}(\lambda)$ and the power law exponent, γ, used to model $b_{bp}(\lambda)$ within a semianalytical inversion algorithm can influence retrieved inherent optical properties [*Werdell et al*., 2013a]. Within this research, we hypothesize that the fixed default values of $S = 0.017$ and $\gamma = 1.0$ used within the SWIM algorithm may have contributed to higher product failure relative to GIOP and QAA. To investigate this, we varied S and γ values within SWIM for a MODIS Aqua test scene of the far northern Great Barrier Reef captured on 22 May 2009 and recorded the number of product failure flags (PRODFAILS) that occurred. Each PRODFAIL flag indicated a pixel for which the SWIM algorithm could not converge to a solution.

Table C1 shows that, relative to the default SWIM parameterization (i.e., $S = 0.017$, $\gamma = 1.0$), the lowest number of SWIM product failures (5719) occurred when $S = 0.025$ and $\gamma = 0.5$, and the largest number of product failures (47,495) occurred when $S = 0.010$ and $\gamma = 1.5$. Figure C1 shows where PRODFAIL pixels occur using three S/γ SWIM parameterizations: (a) default ($S = 0.017$, $\gamma = 1.0$), (b) lowest product failure ($S = 0.025$, $\gamma = 0.5$), and (c) highest product failure ($S = 0.010$, $\gamma = 1.5$). The default parameterization (a) and the lower product failure parameterization (b) exhibit little or no product failure across the continental shelf and into deeper offshore waters apart from over very shallow coral reef structures. Notably, using a parameterization of $S = 0.025$ and $\gamma = 0.5$, product failures appear to be slightly reduced in large north facing bays. Conversely, the highest product failure parameterization (c) exhibits product failure across most of the shallow shelf waters of the test scene, yet yields slightly more valid retrievals in the nearshore region.

From this brief investigation, we conclude that the default parameterization of SWIM can converge to a solution in relatively clear waters, however, it has difficulties in the nearshore region. Nearshore optically complex waters of the Great Barrier Reef are often dominated by suspended sediments and colored dissolved organic matter, CDOM [*Blondeau-Patissier et al*., 2009]. For optically complex waters, previous research has indicated that smaller values of S and γ are more suitable for modeling highly absorbing/scattering waters [*Antoine et al*., 2011; *Blondeau-Patissier et al*., 2009; *Twardowski et al*., 2004]. Thus, we conclude that the SWIM algorithm's parameterization requires refinement in order to reduce product failures in the nearshore region. A band ratio approach similar to that implemented by the QAA [*Lee et al*., 2002] or the adaptive technique of *Brando et al*. [2012] are approaches that, with further work, may improve SWIM's performance in the nearshore; however, such approaches may be confounded in optically shallow waters where the water-leaving radiance signal is influenced by benthic reflectance.

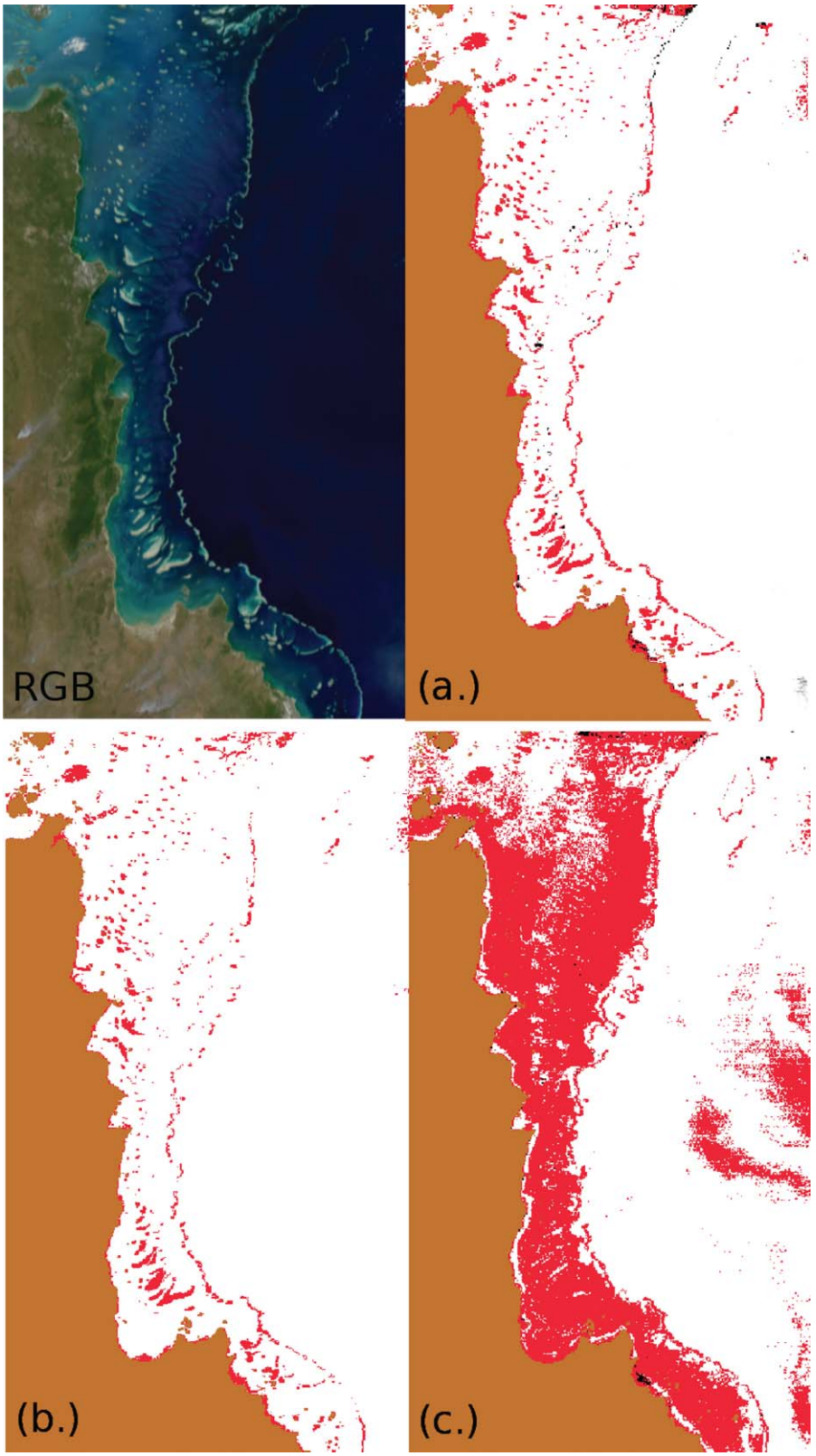

Figure C1. MODIS Aqua scene of the northern Great Barrier Reef captured on 22 May 2009. SWIM algorithm product failures are red pixels, land is brown. RGB: quasi-true color image, (a) standard SWIM parameterization with $S = 0.017$, $\gamma = 1.0$, (b) SWIM parameterization for which the least product failures occurred, $S = 0.025$, $\gamma = 0.5$, and (c) SWIM parameterization for which the most product failures occurred, $S = 0.010$, $\gamma = 1.5$. Product failures in Figure C1b are mostly reduced relative to Figure C1a in the nearshore zone. Note, product failures consistently occur over coral reef structures for which the water column is shallow (<5 m).

Acknowledgments

This research was generously supported by an Australian Research Council Linkage Project Grant (LP100100342), the Great Barrier Reef Foundation, and a NASA Postdoctoral Program Fellowship at Goddard Space Flight Center administered by Oak Ridge Associated Universities. We thank Sean Bailey, John Wilding, and Tommy Owens for their kind support with code development and the handling and processing of large volumes of MODIS Aqua data. We recognize the valuable advice regarding shallow water optics kindly provided by ZhongPing Lee during the early development of this research project. The authors also thank Rodrigo Garcia for his advice regarding implementation of the Levenberg-Marquardt algorithm. We also wish to acknowledge the efforts of the anonymous reviewers for their insightful comments and attention to detail. The IOP data set used in the radiative transfer modeling study can be accessed from the IOCCG's website (http://www.ioccg.org/groups/OCAG_data.html). All MODIS Aqua Level-1A data used are freely available from the NASA Ocean Color website (http://oceancolor.gsfc.nasa.gov/). The 3D-GBR bathymetric data set is freely available from e-Atlas website (http://eatlas.org.au/data/uuid/200aba6b-6fb6–443e-b84b-86b0bbdb53ac), whilst the benthic albedo map can be accessed via PANGEA® earth and environmental science data publishing website (http://doi.pangaea.de/10.1594/PANGAEA.835979).

References

Ahmad, Z., B. A. Franz, C. R. McClain, E. J. Kwiatkowska, J. Werdell, E. P. Shettle, and B. N. Holben (2010), New aerosol models for the retrieval of aerosol optical thickness and normalized water-leaving radiances from the SeaWiFS and MODIS sensors over coastal regions and open oceans, *Appl. Opt.*, *49*(29), 5545–5560, doi:10.1364/AO.49.005545.

Amante, C., and B. W. Eakins (2009), ETOPO1 1 Arc-Minute Global Relief Model: Procedures, data sources and analysis, *NOAA Tech. Memo. NESDIS NGDC-24*, NOAA, Dep. of Commer., Boulder, Colo.

Antoine, D., D. A. Siegel, T. Kostadinov, S. Maritorena, N. B. Nelson, B. Gentili, V. Vellucci, and N. Guillocheaub (2011), Variability in optical particle backscattering in contrasting bio-optical oceanic regimes, *Limnol. Oceanogr.*, *56*(3), 955–973.

Bailey, S. W., B. A. Franz, and P. J. Werdell (2010), Estimation of near-infrared water-leaving reflectance for satellite ocean color data processing, *Opt. Express*, *18*(7), 7521–7527, doi:10.1364/OE.18.007521.

Barnes, B. B., C. Hu, B. A. Schaeffer, Z. Lee, D. A. Palandro, and J. C. Lehrter (2013), MODIS-derived spatiotemporal water clarity patterns in optically shallow Florida Keys waters: A new approach to remove bottom contamination, *Remote Sens. Environ.*, *134*, 377–391, doi:10.1016/j.rse.2013.03.016.

Barnes, B. B., C. Hu, J. P. Cannizzaro, S. E. Craig, P. Hallock, D. L. Jones, J. C. Lehrter, N. Melo, B. A. Schaeffer, and R. Zepp (2014), Estimation of diffuse attenuation of ultraviolet light in optically shallow Florida Keys waters from MODIS measurements, *Remote Sens. Environ.*, *140*, 519–532, doi:10.1016/j.rse.2013.09.024.

Beaman, R. J. (2010), Project 3DGBR: A high-resolution depth model for the Great Barrier Reef and Coral Sea, Marine and Tropical Sciences Research Facility (MTSRF), Project 2.5i.1a, final report, 100 pp., Reef and Rainforest Research Centre (RRRC), Cairns, Queensland, Australia. [Available at http://e-atlas.org.au/content/gbr-jcu-bathymetry-gbr.]

Bierwirth, P. N., T. J. Lee, and R. V. Burne (1993), Shallow sea-floor reflectance and water depth derived by unmixing multispectral imagery, *Photogramm. Eng. Remote Sens.*, *59*(3), 331–338.

Blondeau-Patissier, D., V. E. Brando, K. Oubelkheir, A. G. Dekker, L. A. Clementson, and P. Daniel (2009), Bio-optical variability of the absorption and scattering properties of the Queensland inshore and reef waters, Australia, *J. Geophys. Res.*, *114*, C05003, doi:10.1029/2008JC005039.

Brando, V. E., J. M. Anstee, M. Wettle, A. G. Dekker, S. R. Phinn, and C. Roelfsema (2009), A physics based retrieval and quality assessment of bathymetry from suboptimal hyperspectral data, *Remote Sens. Environ.*, *113*(4), 755–770, doi:10.1016/j.rse.2008.12.003.

Brando, V. E., T. Schroeder, D. Blondeau-Patissier, L. A. Clementson, and A. G. Dekker (2011), Reef rescue marine monitoring program: Using remote sensing for GBR wide water quality, Final report for 2010/11 activities, final report, CSIRO, Canberra, ACT, Australia.

Brando, V. E., A. G. Dekker, Y. J. Park, and T. Schroeder (2012), Adaptive semianalytical inversion of ocean color radiometry in optically complex waters, *Appl. Opt.*, *51*(15), 2808–2833, doi:10.1364/AO.51.002808.

Bricaud, A., A. Morel, and L. Prieur (1981), Absorption by dissolved organic matter of the sea (yellow substance) in the UV and visible domains, *Limnol. Oceanogr.*, *26*(1), 45–53.

Bricaud, A., A. Morel, M. Babin, K. Allali, and H. Claustre (1998), Variations of light absorption by suspended particles with chlorophyll a concentration in oceanic (case 1) waters: Analysis and implications for bio-optical models, *J. Geophys. Res.*, *103*(C13), 31,033–31,044, doi:10.1029/98JC02712.

Brodie, J. E., F. J. Kroon, B. Schaffelke, E. C. Wolanski, S. E. Lewis, M. J. Devlin, I. C. Bohnet, Z. T. Bainbridge, J. Waterhouse, and A. M. Davis (2012), Terrestrial pollutant runoff to the Great Barrier Reef: An update of issues, priorities and management responses, *Mar. Pollut. Bull.*, *65*(4–9), 81–100, doi:10.1016/j.marpolbul.2011.12.012.

Cannizzaro, J. P., and K. L. Carder (2006), Estimating chlorophyll a concentrations from remote-sensing reflectance in optically shallow waters, *Remote Sens. Environ.*, *101*(1), 13–24, doi:10.1016/j.rse.2005.12.002.

Carder, K. L., F. R. Chen, Z. P. Lee, S. K. Hawes, and D. Kamykowski (1999), Semianalytic moderate-resolution imaging spectrometer algorithms for chlorophyll a and absorption with bio-optical domains based on nitrate-depletion temperatures, *J. Geophys. Res.*, *104*(C3), 5403–5421, doi:10.1029/1998JC900082.

Choukroun, S., P. V. Ridd, R. Brinkman, and L. I. W. McKinna (2010), On the surface circulation in the western Coral Sea and residence times in the Great Barrier Reef, *J. Geophys. Res.*, *115*, C06013, doi:10.1029/2009JC005761.

Ciotti, A. M., and A. Bricaud (2006), Retrievals of a size parameter for phytoplankton and spectral light absorption by colored detrital matter from water-leaving radiances at SeaWiFS channels in a continental shelf region off Brazil, *Limnol. Oceanogr. Methods*, *4*, 237–253.

Dekker, A. G., et al. (2011), Intercomparison of shallow water bathymetry, hydro-optics, and benthos mapping techniques in Australian and Caribbean coastal environments, *Limnol. Oceanogr. Methods*, *9*, 396–425, doi:10.4319/lom.2011.9.396.

Devlin, M., and B. Schaffelke (2009), Spatial extent of riverine flood plumes and exposure of marine ecosystems in the Tully coastal region, Great Barrier Reef, *Mar. Freshwater Res.*, *60*(11), 1109–1122, doi:10.1071/MF08343.

Devlin, M., L. W. McKinna, J. G. Álvarez-Romero, C. Petus, B. Abott, P. Harkness, and J. Brodie (2012), Mapping the pollutants in surface riverine flood plume waters in the Great Barrier Reef, Australia, *Mar. Pollut. Bull.*, *65*(4–9), 224–235, doi:10.1016/j.marpolbul.2012.03.001.

Dierssen, H. M., R. C. Zimmerman, R. A. Leathers, T. V. Downes, and C. O. Davis (2003), Ocean color remote sesning of seagrass and bathymetry in the Bahamas Banks by high-resolution airborne imagery, *Limnol. Oceanogr.*, *48*(1, part 2), 444–455.

Doerffer, R., and H. Schiller (2007), The MERIS Case 2 water algorithm, *Int. J. Remote Sens.*, *28*(3-4), 517–535, doi:10.1080/01431160600821127.

Egbert, G. D., and S. Y. Erofeeva (2002), Efficient inverse modeling of barotropic ocean tides, *J. Atmos. Oceanic Technol.*, *19*, 183–204.

ESRI (2011), *ArcGIS Desktop Release 10*, edited, Environ. Syst. Res. Inst., Environ. Res. Syst., Redlands, Calif.

Fabricius, K. E., M. Logan, S. Weeks, and J. Brodie (2014), The effects of river run-off on water clarity across the central Great Barrier Reef, *Mar. Pollut. Bull.*, *84*, 191–200, doi:10.1016/j.marpolbul.2014.05.012.

Fearns, P. R. C., W. Klonowski, R. C. Babcock, P. England, and J. Phillips (2011), Shallow water substrate mapping using hyperspectral remote sensing, *Cont. Shelf Res.*, *31*(12), 1249–1259, doi:10.1016/j.csr.2011.04.005.

Garcia, R. A., P. R. C. S. Fearns, and L. I. W. McKinna (2014a), Detecting trend and seasonal changes in bathymetry derived from HICO imagery: A case study of Shark Bay, Western Australia, *Remote Sens. Environ.*, *147*, 186–205, doi:10.1016/j.rse.2014.03.010.

Garcia, R. A., L. I. W. McKinna, J. D. Hedley, and P. R. C. S. Fearns (2014b), Improving the optimization for a semi-analytical shallow water inversion model in the presence of spectrally correlated noise, *Limnol. Oceanogr. Methods*, *12*, 651–669, doi:10.4319/lom.2014.12.651.

Goodman, J., and S. L. Ustin (2007), Classification of benthic composition in a coral reef environment using spectral unmixing, *J. Appl. Remote Sens.*, *1*(1), 011501, doi:10.1117/1.2815907.

Gordon, H. R., O. B. Brown, R. H. Evans, J. W. Brown, R. C. Smith, K. S. Baker, and D. K. Clark (1988), A semianalytic radiance model of ocean color, *J. Geophys. Res.*, *93*(D9), 10,909–10,924, doi:10.1029/JD093iD09p10909.

Hedley, J. D., C. Roelfsema, and S. R. Phinn (2009), Efficient radiative transfer model inversion for remote sensing applications, *Remote Sens. Environ.*, *113*(11), 2527–2532, doi:10.1016/j.rse.2009.07.008.

Hedley, J. D., C. M. Roelfsema, S. R. Phinn, and P. J. Mumby (2012), Environmental and sensor limitations in optical remote sensing of coral reefs: Implications for monitoring and sensor design, *Remote Sens.*, *4*(1), 271–302.

Hochberg, E. J., M. J. Atkinson, and S. Andréfouët (2003), Spectral reflectance of coral reef bottom-types worldwide and implications for coral reef remote sensing, *Remote Sens. Environ.*, *85*(2), 159–173, doi:10.1016/S0034–4257(02)00201-8.

IOCCG (2000), Remote sensing of ocean colour in coastal and other optically-complex waters, Report No. 3, IOCCG, Dartmouth, Nova Scotia, Canada.

IOCCG (2006), Remote sensing of inherent optical properties: Fundamentals, tests of algorithms and applications, Report No. 5, IOCCG, Dartmouth, Nova Scotia, Canada.

Jolliff, J. K., J. C. Kindle, I. Shulman, B. Penta, M. A. M. Friedrichs, R. Helber, and R. A. Arnone (2009), Summary diagrams for coupled hydrodynamic-ecosystem model skill assessment, *J. Mar. Syst.*, *76*(1–2), 64–82, doi:10.1016/j.jmarsys.2008.05.014.

Klonowski, W. M., P. R. Fearns, and M. J. Lynch (2007), Retrieving key benthic cover types and bathymetry from hyperspectral imagery, *J. Appl. Remote Sens.*, *1*(1), 011505, doi:10.1117/1.2816113.

Lee, Z., and K. L. Carder (2002), Effect of spectral band numbers on the retrieval of water column and bottom properties from ocean color data, *Appl. Opt.*, *41*(12), 2191–2201, doi:10.1364/AO.41.002191.

Lee, Z., K. L. Carder, C. D. Mobley, R. G. Steward, and J. S. Patch (1998), Hyperspectral remote sensing for shallow waters. I. A semianalytical model, *Appl. Opt.*, *37*(27), 6329–6338, doi:10.1364/AO.37.006329.

Lee, Z., K. L. Carder, C. D. Mobley, R. G. Steward, and J. S. Patch (1999), Hyperspectral remote sensing for shallow waters. 2. Deriving bottom depths and water properties by optimization, *Appl. Opt.*, *38*(18), 3831–3843, doi:10.1364/AO.38.003831.

Lee, Z., K. L. Carder, R. F. Chen, and T. G. Peacock (2001), Properties of the water column and bottom derived from Airborne Visible Infrared Imaging Spectrometer (AVIRIS) data, *J. Geophys. Res.*, *106*(C6), 11,639–11,651, doi:10.1029/2000JC000554.

Lee, Z., K. L. Carder, and R. A. Arnone (2002), Deriving inherent optical properties from water color: A multiband quasi-analytical algorithm for optically deep waters, *Appl. Opt.*, *41*(27), 5755–5772, doi:10.1364/AO.41.005755.

Lee, Z., K. Du, and R. Arnone (2005), A model for the diffuse attenuation coefficient of downwelling irradiance, *J. Geophys. Res.*, *110*, C02016, doi:10.1029/2004JC002275.

Lee, Z., C. Hu, B. Casey, S. Shang, H. Dierssen, and R. Arnone (2010), Global shallow water bathymetry from satellite ocean color data, *Eos Trans. AGU*, *91*(46), 429–430, doi:10.1029/2010EO460002.

Leiper, I., S. Phinn, and A. G. Dekker (2011), Spectral reflectance of coral reef benthos and substrate assemblages on Heron Reef, Australia, *Int. J. Remote Sens. 33*(12), 3946–3965, doi:10.1080/01431161.2011.637675.

Lesser, M. P., and C. D. Mobley (2007), Bathymetry, water optical properties, and benthic classification of coral reefs using hyperspectral remote sensing imagery, *Coral Reefs*, *26*(4), 819–829, doi:10.1007/s00338-007-0271-5.

Louchard, E. M., R. P. Reid, F. C. Stephens, C. O. Daviss, R. A. LEathers, and T. V. Downes (2003), Optical remote sensing of benthic habitats and bathymetry in coastal environments at Lee Stocking Island, Bahamas: A comparative spectra classification approach, *Limnol. Oceanogr.*, *48*(1, part 2), 511–551.

Lourakis, M. I. A. (2003), Levmar: Levenberg-Marquardt nonlinear least squares algorithm in C/C++. [Available at http://www.ics.forth.gr/~lourakis/levmar/.]

Lyzenga, D. R. (1978), Passive remote sensing techniques for mapping water depth and bottom features, *Appl. Opt.*, *17*(3), 379–383, doi:10.1364/AO.17.000379.

Maritorena, S., A. Morel, and B. Gentili (1994), Diffuse relfectance of oceanic shallow waters: Influence of water depth and bottom albedo, *Limnol. Oceanogr.*, *39*(7), 1689–1703.

Maritorena, S., D. A. Siegel, and A. R. Peterson (2002), Optimization of a semianalytical ocean color model for global-scale applications, *Appl. Opt.*, *41*(15), 2705–2714, doi:10.1364/AO.41.002705.

Matthews, E. J., A. D. Heap, and M. Woods (2007), *Inter-Reefal Seabed Sediments and Geomorphology of the Great Barrier Reef, A Spatial Analysis*, Record 2007/09, edited, p. 140, Geosci. Aust., Canberra.

McClain, C. R. (2009), A decade of satellite ocean color observations, *Annu. Rev. Mar. Sci.*, *1*(1), 19–42, doi:10.1146/annurev.marine.010908.163650.

Mitchell, B. G. (1990), Algorithms for determining the absorption coefficient for aquatic particulates using the quantitative filter technique, *Proc. SPIE Soc. Opt. Eng.*, *1302*, 137–148.

Mitchell, B. G., M. M. Kahru, J. Wieland, and M. Stramska (2002), Determination of spectral absorption coefficients of particles, dissolved material and phytoplankton for discrete water samples, in *Ocean Optics Protocols for Satellite Ocean Color Sensor Validation, TM-2003–211621, Rev. 4*, vol IV, edited by J. L. Mueller, G. S. Fargion, and C. R. McClain, pp. 39–64, NASA, Greenbelt, Md.

Mobley, C. D., and L. K. Sundman (2003), Effects of optically shallow bottoms on upwelling radiances: Inhomogeneous and sloping bottoms, *Limnol. Oceanogr.*, *48*(1, part 2), 329–336.

Mobley, C. D., and L. K. Sundman (2008), *Hydrolight 5 Ecolight 5 Users' Guide*, Sequoia Sci., Bellvue, Wash.

Mobley, C. D., et al. (2005), Interpretation of hyperspectral remote-sensing imagery by spectrum matching and look-up tables, *Appl. Opt.*, *44*(17), 3576–3592, doi:10.1364/AO.44.003576.

Moré, J. J. (1977), The Levenberg-Marquardt algorithm: Implementation and theory, in *Lecture Notes in Mathematics*, vol. 630, edited by G. A. Watson, pp. 105–116, Springer, Berlin.

Morel, A., D. Antoine, and B. Gentili (2002), Bidirectional reflectance of oceanic waters: Accounting for Raman emission and varying particle scattering phase function, *Appl. Opt.*, *41*(30), 6289–6306, doi:10.1364/AO.41.006289.

Mueller, J. L., R. W. Austin, A. Andre Morel, G. S. Fargion, and C. R. McClain (2003), Introduction, background and conventions, in Ocean Optics Protocols for Satellite Ocean Color Sensor Validation, TM-2003–211621, Rev. 4, vol. I, edited by J. L. Mueller, G. S. Fargion, and C. R. McClain, NASA, Greenbelt, Md.

NASA (2012), Pre-Aerosol, Clouds, and Ocean Ecosystem (PACE) Mission, Science Definition Team Report, report, NASA, Greenbelt, Md. [Available at http://decadal.gsfc.nasa.gov/pace.html.]

O'Reilly, J. E., S. Maritorena, B. G. Mitchell, D. A. Siegel, K. L. Carder, S. A. Garver, M. Kahru, and C. McClain (1998), Ocean color chlorophyll algorithms for SeaWiFS, *J. Geophys. Res.*, *103*(C11), 24,937–24,953, doi:10.1029/98JC02160.

Orpin, A. R., and P. V. Ridd (2012), Exposure of inshore corals to suspended sediments due to wave-resuspension and river plumes in the central Great Barrier Reef: A reappraisal, *Cont. Shelf Res.*, *47*, 55–67, doi:10.1016/j.csr.2012.06.013.

Petus, C., E. T. da Silva, M. Devlin, A. S. Wenger, and J. G. Álvarez-Romero (2014), Using MODIS data for mapping of water types within river plumes in the Great Barrier Reef, Australia: Towards the production of river plume risk maps for reef and seagrass ecosystems, *J. Environ. Manage.*, *137*, 163–177, doi:10.1016/j.jenvman.2013.11.050.

Philpot, W. D. (1987), Radiative transfer in stratified waters: A single-scattering approximation for irradiance, *Appl. Opt.*, *26*(19), 4123–4132, doi:10.1364/AO.26.004123.

Philpot, W. D. (1989), Bathymetric mapping with passive multispectral imagery, *Appl. Opt.*, *28*(8), 1569–1578, doi:10.1364/AO.28.001569.

Pitcher, C. R., et al. (2007), Seabed biodiversity on the continental shelf of the Great Barrier Reef world heritage area, AIMS/CSIRO/QM/QDPI/CRC Reef Research Task Final Report, final report, 320 pp., CSIRO Mar. and Atmos. Res., Cleveland, QLD, Australia.

Pope, R. M., and E. S. Fry (1997), Absorption spectrum (380–700 nm) of pure water. II. Integrating cavity measurements, *Appl. Opt.*, *36*(33), 8710–8723, doi:10.1364/AO.36.008710.

Qin, Y., V. E. Brando, A. G. Dekker, and D. Blondeau-Patissier (2007), Validity of SeaDAS water constituents retrieval algorithms in Australian tropical coastal waters, *Geophys. Res. Lett.*, *34*, L21603, doi:10.1029/2007GL030599.

Reichstetter, M., L. McKinna, P. Fearns, S. Weeks, C. Roelfsema, and M. Furnas (2014), Seafloor brightness map of the Great Barrier Reef, Australia, derived from biodiversity data, PANGAEA, doi:10.1594/PANGAEA.835979.

Roelfsema, C. M., and S. R. Phinn (2012), Spectral reflectance library of selected biotic and abiotic coral reef features in Heron Reef, PANGAEA, doi:10.1594/PANGAEA.804589.

Roesler, C. S., M. J. Perry, and K. L. Carder (1989), Modeling in situ phytoplankton absorption from total absorption spectra in productive inland marine waters, *Limnol. Oceanogr.*, *34*(8), 1510–1523.

Schroeder, T., M. J. Devlin, V. E. Brando, A. G. Dekker, J. E. Brodie, L. A. Clementson, and L. McKinna (2012), Inter-annual variability of wet season freshwater plume extent into the Great Barrier Reef lagoon based on satellite coastal ocean colour observations, *Mar. Pollut. Bull.*, *65*(4–9), 210–223, doi:10.1016/j.marpolbul.2012.02.022.

Smyth, T. J., G. F. Moore, T. Hirata, and J. Aiken (2006), Semianalytical model for the derivation of ocean color inherent optical properties: Description, implementation, and performance assessment, *Appl. Opt.*, *45*(31), 8116–8131, doi:10.1364/AO.45.008116.

Stumpf, R. P., K. Holderied, and M. Sinclair (2003), Determination of water depth with high resolution satellite imagery over variable bottom types, *Limnol. Oceanogr.*, *48* (1, part 2), 546–556.

Taylor, K. E. (2001), Summarizing multiple aspects of model performance in a single diagram, *J. Geophys. Res.*, *106*(D7), 7183–7192, doi:10.1029/2000JD900719.

Twardowski, M. S., E. Boss, J. M. Sullivan, and P. L. Donaghay (2004), Modeling the spectral shape of absorption by chromophoric dissolved organic matter, *Mar. Chem.*, *89*(1–4), 69–88, doi:10.1016/j.marchem.2004.02.008.

Weeks, S., P. J. Werdell, B. Schaffelke, M. Canto, Z. Lee, J. Wilding, and G. Feldman (2012), Satellite-derived photic depth on the Great Barrier Reef: Spatio-temporal patterns of water clarity, *Remote Sens.*, *4*(12), 3781–3795.

Werdell, P. J., and C. S. Roesler (2003), Remote assessment of benthic substrate composition in shallow waterws using multispectral reflectance, *Limnol. Oceanogr.*, *48*(1, part 2), 557–567.

Werdell, P. J., B. A. Franz, and S. W. Bailey (2010), Evaluation of shortwave infrared atmospheric correction for ocean color remote sensing of Chesapeake Bay, *Remote Sens. Environ.*, *114*, 2238–2247, doi:10.1016/j.rse.2010.04.027.

Werdell, P. J., et al. (2013a), Generalized ocean color inversion model for retrieving marine inherent optical properties, *Appl. Opt.*, *52*(10), 2019–2037, doi:10.1364/AO.52.002019.

Werdell, P. J., B. A. Franz, J. T. Lefler, W. D. Robinson, and E. Boss (2013b), Retrieving marine inherent optical properties from satellites using temperature and salinity-dependent backscattering by seawater, *Opt. Express*, *21*(26), 32,611–32,622, doi:10.1364/OE.21.032611.

Westberry, T. K., E. Boss, and Z. Lee (2013), Influence of Raman scattering on ocean color inversion models, *Appl. Opt.*, *52*(22), 5552–5561, doi:10.1364/AO.52.005552.

Wettle, M., and V. E. Brando (2006), SAMBUCA – Semi-analytical model for Bathymetry, un-mixing and concentration assessment, CSIRO Land and Water Science Report No. 22/06, CSIRO, Canberra, ACT, Australia.

Zhang, X., L. Hu, and M.-X. He (2009), Scattering by pure seawater: Effect of salinity, *Opt. Express*, *17*(7), 5698–5710, doi:10.1364/OE.17.005698.

Zhao, J., B. Barnes, N. Melo, D. English, B. Lapointe, F. Muller-Karger, B. Schaeffer, and C. Hu (2013), Assessment of satellite-derived diffuse attenuation coefficients and euphotic depths in south Florida coastal waters, *Remote Sens. Environ.*, *131*, 38–50, doi:10.1016/j.rse.2012.12.009.